Strategies to improve the signal and noise performance of active matrix, flat-panel imagers for diagnostic x-ray applications

L. E. Antonuk,[a] K.-W. Jee, Y. El-Mohri, M. Maolinbay, S. Nassif, X. Rong, Q. Zhao, and J. H. Siewerdsen[b]
Department of Radiation Oncology, University of Michigan Medical Center, Ann Arbor, Michigan 48109[c]

R. A. Street
Xerox Palo Alto Research Center, Palo Alto, California 94304

K. S. Shah
Radiation Monitoring Devices, Watertown, Massachusetts 02172

A theoretical investigation of factors limiting the detective quantum efficiency (DQE) of active matrix flat-panel imagers (AMFPIs), and of methods to overcome these limitations, is reported. At the higher exposure levels associated with radiography, the present generation of AMFPIs is capable of exhibiting DQE performance equivalent, or superior, to that of existing film-screen and computed radiography systems. However, at exposure levels commonly encountered in fluoroscopy, AMFPIs exhibit significantly reduced DQE and this problem is accentuated at higher spatial frequencies. The problem applies both to AMFPIs that rely on indirect detection as well as direct detection of the incident radiation. This reduced performance derives from the relatively large magnitude of the square of the total additive noise compared to the system gain for existing AMFPIs. In order to circumvent these restrictions, a variety of strategies to decrease additive noise and enhance system gain are proposed. Additive noise could be reduced through improved preamplifier, pixel and array design, including the incorporation of compensation lines to sample external line noise. System gain could be enhanced through the use of continuous photodiodes, pixel amplifiers, or higher gain x-ray converters such as lead iodide. The feasibility of these and other strategies is discussed and potential improvements to DQE performance are quantified through a theoretical investigation of a variety of hypothetical 200 μm pitch designs. At low exposures, such improvements could greatly increase the magnitude of the low spatial frequency component of the DQE, rendering it practically independent of exposure while simultaneously reducing the falloff in DQE at higher spatial frequencies. Furthermore, such noise reduction and gain enhancement could lead to the development of AMFPIs with high DQE performance which are capable of providing both high resolution radiographic images, at $\sim$100 μm pixel resolution, as well as variable resolution fluoroscopic images at 30 fps. © *2000 American Association of Physicists in Medicine.* [S0094-2405(00)01302-X]

Key words: active matrix flat-panel imager, cascaded systems analysis, diagnostic x-ray imaging, fluoroscopy, indirect detection, direct detection

I. INTRODUCTION

After over a decade of intense development,[1–3] active matrix flat-panel imagers (AMFPIs) are on the threshold of widespread introduction into the clinical environment for applications in radiography, fluoroscopy, mammography, and radiotherapy. While such imagers offer many advantages, it is interesting to examine limitations of AMFPI systems whose design specifications are consistent with the current state of the technology. In particular, this paper contains a detailed examination of the nature and origin of performance limitations of current AMFPI systems operated under conditions of low diagnostic x-ray exposure. A variety of strategies for overcoming these limitations, focusing on the reduction in total additive noise and enhancement of system gain, are discussed. (Additive noise corresponds to the noise of the imaging system in the absence of radiation. In addition, for the purposes of this paper, system gain is defined as the number of imaging quanta output by the imager per pixel, per incident x ray.) The results of a theoretical investigation of the potential performance improvements to be realized over current systems through incorporation of such strategies is reported, and prospects for the realization of such improvements in the future are discussed.

II. TECHNICAL BACKGROUND AND LIMITATIONS OF AMFPI DEVICES

A. Indirect detection and direct detection imagers

AMFPI technology is based on large glass substrates on which imaging pixels are deposited. The term ''active matrix'' refers to the fact that the pixels are arranged in a regu-
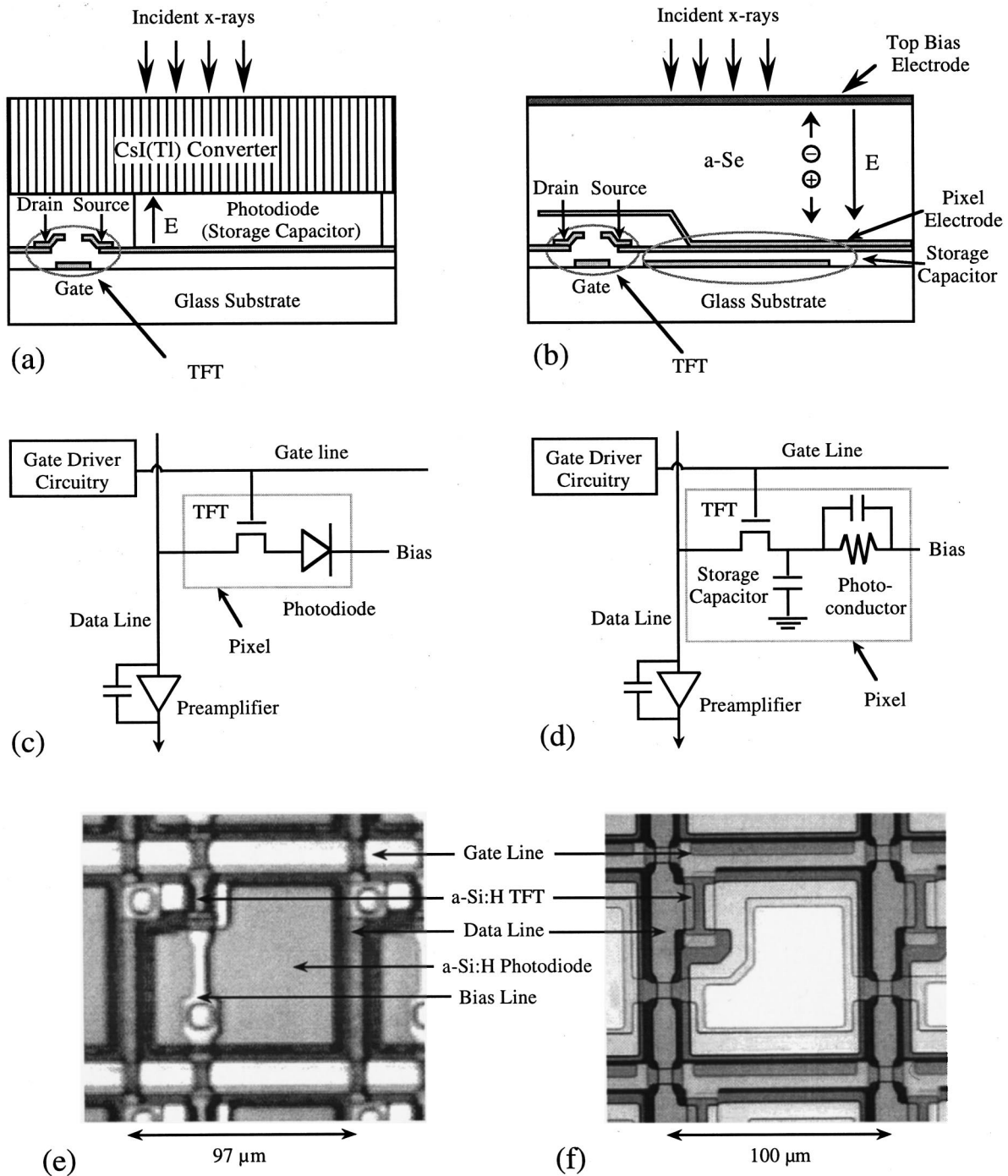
FIG. 1. Illustration highlighting the similarities and differences between indirect detection AMFPIs (a,c,e) and direct detection AMFPIs (b,d,f). (a,b) Schematic diagram showing a side view of incident radiation interacting with an array pixel. (c,d) Equivalent circuit of an array pixel along with gate driver and preamplifier electronics. (e,f) Microphotographs of 97 μm pitch and 100 μm pitch pixels for indirect detection (Ref. 2) and direct detection (Ref. 41), respectively.

lar two-dimensional grid with each pixel containing an amorphous silicon (a-Si:H) based thin-film switch; either a thin-film transistor (TFT), a single diode, or a pair of diodes. In all cases, the pixel switch is connected to some form of pixel storage capacitor that serves to hold an imaging charge induced by the incident radiation.

This imaging technology may be generally divided into two categories, ''indirect'' and ''direct'' detection AMFPIs,

which differ in terms of the method of x-ray detection. Distinguishing features of the two approaches are illustrated in Fig. 1. In indirect detection systems[1] such as shown in Fig. 1(a), a photosensitive element (typically a discrete photodiode) is built into each pixel and incident x rays interact in a scintillating converter [e.g., Gd_2O_2S:Tb or CsI(Tl)] positioned or deposited over the array. These interactions result in the generation of visible light photons. Some of the light

quanta emitted from the scintillator strike the photodiodes where they are converted, typically with high efficiency, into imaging charge (electron–hole pairs). Each photodiode also serves as the pixel storage capacitor. In direct detection systems[4,5] such as illustrated in Fig. 1(b), the active matrix is covered with a thick photoconductive layer (e.g., amorphous selenium [a-Se]) in which incident x rays directly generate imaging charge. Although the photoconductive layer provides capacitance, the imaging charge is stored in a separate storage capacitor built into each pixel. This additional capacitor provides a larger range of signal storage than would be offered by the photoconductive layer alone and helps to protect the pixel switch from potentially deleterious effects associated with the high voltage applied across the photoconductor.

The signal capacity of the pixel, Q_{max}, is given by the product of the pixel storage capacitance, $C_{storage}$, and the voltage across this capacitor, $V_{storage}$,

$$Q_{max} = C_{storage} V_{storage}. \qquad (1)$$

For an indirect detection AMFPI, $V_{storage}$ corresponds to the voltage applied across the photodiode. For a direct detection AMFPI, $V_{storage}$ is initially zero and increases in proportion to the size of the charge that accumulates in the capacitor. For both direct and indirect detection devices, if the array is designed to collect negative charge in the storage capacitors, then a negative voltage will build up across the TFT from the storage capacitor to the data line as charge accumulates. In this case, it is essential that the magnitude of this voltage remains at least $\sim$2 V less than the magnitude of the negative voltage used to keep the pixel TFTs nonconducting ($V_{TFT-OFF}$), in order to insure no leakage of signal through the transistors.[6] In practice, a practical limit for $V_{TFT-OFF}$ imposed by TFT design is just beyond -10 V. In addition if the magnitude of $V_{storage}$ exceeds $\sim$10 V, then indirect detection photodiodes (irrespective of the sign of the collected charge) and the pixel TFTs for indirect or direct detection (for positive collected charge) will begin to exhibit significant leakage current. These considerations imply that the maximum magnitude for $V_{storage}$, consistent with good array performance, is approximately 10 V.

Figures 1(c) and 1(d) illustrate equivalent circuits while Figs. 1(e) and 1(f) contain microphotographs of indirect and direct detection pixels, respectively. In both cases, addressing of the individual pixels is performed via a system of gate and data address lines. Signal integration in the pixel storage capacitors is accomplished by keeping all the pixel switches nonconducting via external voltage switching circuits (gate drivers) attached to the gate lines. Signal readout is performed by using the gate drivers to render the pixel switches conducting, one gate line at a time for full resolution readout or several lines at a time for faster image readout at lower resolution. External preamplifier circuits located at the end of the data lines sample the stored signals from the addressed pixels by integrating the resulting current flow along each data line. After integration, amplification and digitization, these signals are organized into a two-dimensional matrix of values representing a digital image (one value per array pixel

in the case of full resolution readout). Finally, the action of reading out the pixels also reinitializes the pixel storage capacitors, although the presence of blocking layers in some direct detection designs[5] or the use of switching diodes[7] may necessitate other additional initializing actions.

Two important parameters in the design of an AMFPI array are the geometric fill factor and the collection fill factor. The geometric fill factor is the fraction of the pixel area occupied by the pixel storage capacitor. The magnitude of the pixel storage capacitance, $C_{storage}$, is given by the product of the geometric fill factor, the area of the pixel, a_{pix}^2, the capacitor's dielectric constant, and the permittivity of free space divided by the thickness of the dielectric. The definition of the collection fill factor, f_{coll}, which is associated with the reception of secondary quanta, depends upon the means of x-ray detection. For indirect detection AMFPIs, the optical collection fill factor is defined as the fraction of the pixel area for which incident light is transformed with high efficiency into useful signal. In the case of discrete photodiode designs this corresponds to the optically sensitive area of the photodiode. For direct detection, the collection fill factor is the fraction of the pixel area for which charge generated in the overlying photoconductor is collected. For both types of AMFPIs, the symbol a_{coll}^2 is used to designate the area corresponding to the collection fill factor (where $a_{coll}^2 = a_{pix}^2 f_{coll}$).

B. DQE performance of current AMFPI devices

AMFPI technology is of considerable interest for clinical and nonclinical applications for a variety of reasons including (a) real-time digital readout, at up to $\sim$30 fps for some designs; (b) the very large detector areas, comparable to the dimensions of human anatomy (e.g., 29.4×40.6 cm^2 arrays with 2904×3200 pixels[8]), and the highly compact packaging, approaching that of a film cassette, that can be achieved; and (c) the absence of various image-degrading factors affecting other technologies such as developer artifacts in film and veiling glare in x-ray image intensifier systems. In addition, for some applications (e.g., radiography), there is also the possibility of significant performance gains over existing technologies. Such improvements may be quantified through a widely accepted metric of imager performance called the detective quantum efficiency (DQE) which describes the ability of an imager to transfer information from the input of the system to the output. DQE may formally be defined as the square of the signal-to-noise ratio (SNR) at the output of the system divided by the square of the SNR at the input of the system.

In recent years, it has been demonstrated[9,10] that empirical determinations of the frequency-dependent DQE for indirect and direct detection AMFPIs can be reproduced to a reasonable degree of accuracy by theoretical calculations based on a cascaded systems formalism.[11] In this formalism, an imaging system is conceptually divided into a series of stages with each stage characterized by a gain, a noise or a spreading factor. Cascaded systems model calculations indicate that for diagnostic x-ray imaging applications where the exposure to the detector is relatively large (e.g., radiography), the
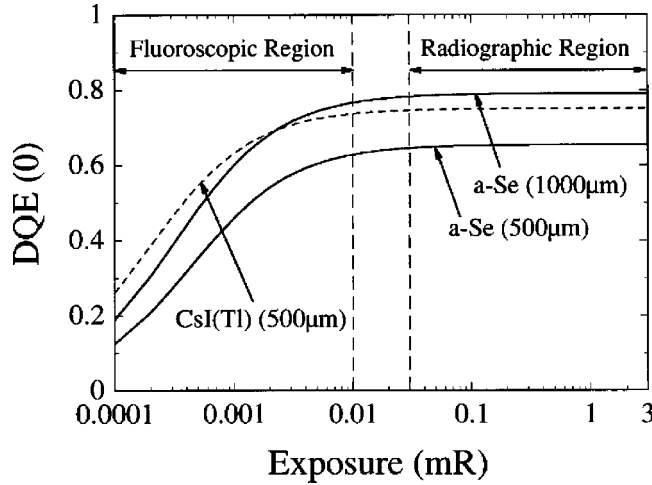
FIG. 2. Plot of theoretical cascaded-systems calculations of zero-frequency DQE for three hypothetical, 200 μm pitch active matrix flat-panel imagers whose designs are consistent with existing AMFPI technology. Results are shown for an indirect detection AMFPI utilizing discrete photodiodes and coupled to 500 μm of CsI(Tl); and direct detection AMFPIs coupled to 500 μm and 1000 μm thick layers of *a*-Se. The AMFPI designs are assumed to incorporate a pixel switch based on a TFT, as is the case for all calculations appearing in this paper. The calculations, performed at 80 kVp, are shown as a function of exposure. The dashed vertical lines indicate ranges of exposure for the fluoroscopic and radiographic applications.

DQE for both indirect[12] and direct[13] detection AMFPIs can be significantly higher than that of conventional technologies (e.g., film–screen and storage phosphor systems). However, these same models consistently predict a substantial falloff in DQE with decreasing exposure over the range of operation typically associated with fluoroscopy ($\sim$0.1 to 10 μR). (In this paper, all exposures refer to exposure to the detector.)

This falloff is illustrated in Fig. 2 which shows theoretical calculations of the zero-frequency DQE over fluoroscopic and radiographic exposures for a pair of hypothetical imagers; an indirect detection AMFPI [with 500 μm of CsI(Tl) (Ref. 14)] and a direct detection AMFPI [with 500 μm of *a*-Se (Ref. 13)]. The calculations [based on Eq. (2) appearing below] were performed for a pixel-to-pixel pitch of 200 μm corresponding to that being pursued by a number of groups for fluoroscopy.[7,14–16] The input parameters used in the calculations correspond to hypothetical conventional AMFPI designs whose design specifications are representative of the current state of the technology. (Input parameters for conventional AMFPIs are summarized in Sec. IV.) These calculations illustrate the falloff in DQE that begins in the middle of the fluoroscopic range. Even a substantial increase in the thickness of the *a*-Se converter to 1000 μm (Ref. 17) does not eliminate this falloff, as demonstrated in the figure. A similar falloff in DQE is observed at higher spatial frequencies where the decline starts at progressively higher exposures.[13,15]

The origin of this reduction in detective quantum efficiency may be understood by examining the cascaded systems expression for the zero-frequency DQE for AMFPI systems. Due to the high degree of parallelism between indirect and direct detection AMFPIs, as is illustrated in Fig. 1, this expression may be written in a form applicable to both systems,

$$
\text{DQE}(0) = \frac{\bar{g}_1 \bar{g}_k \bar{g}_4}{1 + \bar{g}_4(\bar{g}_k + \varepsilon_{g_k}) + \dfrac{\sigma_{\text{add}}^2}{a_{\text{coll}}^2 \bar{q}_0 \bar{g}_1 \bar{g}_k \bar{g}_4}}
$$

$$
= \frac{\bar{g}_1 \bar{g}_k \bar{g}_4}{1 + \bar{g}_4(\bar{g}_k + \varepsilon_{g_k}) + \dfrac{\sigma_{\text{add}}^2}{a_{\text{pix}}^2 \bar{q}_0 \bar{g}_1 \bar{g}_k \bar{g}_4 f_{\text{coll}}}}. \quad (2)
$$

The symbols appearing in Eq. (2), and for other cascaded systems expressions used in this paper, are defined in Table I. In addition, the subscript k in Eq. (2) represents stage 2 or stage 3 for indirect or direct detection systems, respectively. Moreover, the square of the total additive noise (σ_{add}) may be written in the form,[18]

$$
\sigma_{\text{add}}^2 = \sigma_{\text{TFT−thermal}}^2 + \sigma_{\text{amp}}^2 + \sigma_{\text{ext-line}}^2 + \sigma_{\text{shot}}^2 + \sigma_{1/f}^2 + \sigma_{\text{ADC}}^2, \quad (3)
$$

where the expression includes contributions from TFT thermal noise ($\sigma_{\text{TFT-thermal}}$), external preamplifier noise (σ_{amp}), external line noise ($\sigma_{\text{ext-line}}$), shot (σ_{shot}) and flicker ($\sigma_{1/f}$) noise associated with the pixels, and ADC noise (σ_{ADC}).

Of particular interest in Eq. (2) is the term in the denominator containing the ratio of σ_{add}^2 to the product of the pixel area (a_{pix}^2), the mean x-ray fluence ($\bar{q}_0$), and the average system gain ($\bar{g}_1 \bar{g}_k \bar{g}_4 f_{\text{coll}}$). At large exposures (large $\bar{q}_0$), the contribution of this term is minimized and DQE(0) will be a maximum. As the exposure decreases, the influence of this term upon the DQE(0) depends upon the ratio of σ_{add}^2 to $\bar{g}_1 \bar{g}_k \bar{g}_4 f_{\text{coll}}$. If this ratio is sufficiently small, the magnitude of the third term in the denominator of Eq. (2) remains unimportant and good DQE(0) is maintained. Otherwise, the DQE(0) will steadily fall with decreasing exposure. Similarly, for a given exposure, DQE(0) will fall if the additive noise becomes large enough that the magnitude of the third term becomes significant in the denominator. These considerations apply equally to nonzero spatial frequencies, the expressions for which contain dependencies similar to that of Eq. (2)[13,19] [also, see Eqs. (6a) and (6b) in Sec. IV].

To quantify these considerations, the cases of AMFPIs employing CsI(Tl) and *a*-Se converters are considered. System gains ($\bar{g}_1 \bar{g}_k \bar{g}_4 f_{\text{coll}}$) on the order of 10^3 electrons per pixel, per x ray [for up to 610 μm of CsI(Tl) at $\sim$75 kVp (Refs. 2, 7, 14)] and $\sim$600 electrons per pixel, per x ray [for 500 μm of *a*-Se at 80 kVp (Ref. 15)] have been reported for present generation indirect and direct detection devices, respectively. Moreover, additive noise levels of $\sim 10^3 e$ [rms] also appear achievable for present generation AMFPIs.[7,20] At low fluoroscopic exposures, the number of incident x rays per 200 μm pixel approaches unity[9] and the value of the second term in the denominator of Eq. (2) is on the order of 10^3. In order to have high DQE, the ratio of σ_{add}^2 to $\bar{g}_1 \bar{g}_k \bar{g}_4 f_{\text{coll}}$ should be sufficiently small so as to make the third term in the denominator negligible. However, for present AMFPI designs, this ratio is about 1000–2000 which directly leads, under fluoroscopic conditions, to steep decreases in DQE with either diminishing exposure, as illustrated in Fig. 2, or increasing additive noise.[9,10,12]

TABLE I. Glossary of terms and symbols relevant to cascaded systems modeling of indirect and direct detection AMFPIs. The descriptions of the various cascaded system stages are as per Refs. 9 and 13 for the indirect detection and direct detection systems, respectively.

| State # in cascaded systems representation of imager | |
Indirect detection	Direct detection
$i=0$ X-ray quanta incident on imager	X-ray quanta incident on imager
$i=1$ Interaction of x rays in scintillator	Interaction of x rays in photoconductor
$i=2$ Generation and emission of optical quanta	Spatial spreading of x-ray energy deposition
$i=3$ Spatial spreading of optical quanta	Generation of electron–hole pairs
$i=4$ Coupling of optical quanta to detector elements	Collection of electronic quanta
$i=5$ Integration of optical quanta by photodiodes	Integration of electronic quanta by pixel electrodes
$i=6$ Additive noise	Additive noise

| Imaging system parameters | |
Indirect detection	Direct detection
$\bar{q}_0$ Incident x-ray fluence (x rays/mm^2)	$\bar{q}_0$ Incident x-ray fluence (x rays/mm^2)
$\bar{g}_1$ Quantum detection efficiency of scintillator	$\bar{g}_1$ Quantum detection efficiency of photoconductor
$\bar{g}_2$ Quantum gain of scintillator	T_2 Inherent photoconductor MTF
ϵ_{g_2} Poisson excess in $\bar{g}_2$	$\bar{g}_3$ Quantum gain of photoconductor
T_3 X-ray converter MTF	ϵ_{g_3} Poisson excess in $\bar{g}_3$
$\bar{g}_4$ Coupling efficiency of photodiode	$\bar{g}_4$ Collection efficiency of photoconductor
a_{pix}^2 Area of the pixel (mm^2)	a_{pix}^2 Area of the pixel (mm^2)
a_{coll}^2 Area corresponding to the optical collection fill factor, f_{coll}, of a photodiode array (mm^2)	a_{coll}^2 Area corresponding to the collection fill factor, f_{coll}, of a photoconductor array (mm^2)
T_5 MTF corresponding to a_{coll}	T_5 MTF corresponding to a_{coll}

Empirical and theoretical performance parameters
(u,v) Spatial frequency coordinates (mm^{-1})
MTF Modulation transfer function
NPS Noise power spectrum
DQE Detective quantum efficiency

III. STRATEGIES TO IMPROVE AMFPI PERFORMANCE

From the preceding analysis, it is anticipated that strategies which reduce the ratio of the total additive noise squared, σ_{add}^2, to the system gain, $\bar{g}_1 \bar{g}_k \bar{g}_4 f_{\text{coll}}$, should lead to improved DQE performance for AMFPI systems. The remainder of this section explores various avenues for decreasing total additive noise (and thus σ_{add}^2) and increasing system gain.

A. Reduction of additive noise

For the purposes of this paper, it is assumed that high quality arrays and properly designed acquisition electronics are incorporated into conventional AMFPI systems so that the noise contribution from the final three terms in Eq. (3) is negligible. In this case, the dominant noise components will be the thermal noise of the pixel TFT, the preamplifier noise, and the line noise.

TFT thermal noise is given by

$$\sigma_{\text{TFT-thermal}} = \sqrt{2kTC_{\text{storage}}}, \qquad (4)$$

where k is the Boltzmann constant and T is the temperature in degrees Kelvin. Significant reductions in thermal noise through temperature decreases are unlikely given that lowering T more than 20 K significantly increases the on-resistance of the pixel TFTs, thereby slowing down readout speed, and good transistor operation is precluded below $\sim$250 K. Therefore, any thermal noise reductions must de-

rive from diminution of C_{storage}. However, the value of C_{storage} must also be chosen so as to allow storage of the largest signal size associated with the application. In the case of indirect detection AMFPIs where the storage capacitor is also the a-Si:H photodiode, and given the desirability of maximizing photodiode area (so as to maximize gain), the thickness of the photodiode is the only free parameter for adjusting C_{storage}. The minimum photodiode thickness compatible with good optical efficiency is $\sim$0.5 μm while the maximum photodiode thickness presently used is $\sim$1.5 μm (Ref. 6), corresponding to a capacitance of $\sim$2.1 pF and $\sim$0.71 pF per 100 μm^2, respectively. Further refinements in the processing techniques used to make large-area arrays could conceivably allow $\sim$3 μm a-Si:H layers, corresponding to $\sim$0.35 pF per 100 μm^2. For direct detection AMFPIs, although the storage capacitor can in principle be made quite small, C_{storage} must be kept sufficiently large so as to insure adequate signal storage capacity at a voltage (V_{storage}) below the threshold at which leakage through the pixel TFTs becomes a concern (see Sec. II A). Therefore, minimizing C_{storage}, and thus $\sigma_{\text{TFT-thermal}}$, involves various considerations relating to the array design and imaging application. This is further explored in Sec. IV.

Another promising candidate for additive noise reduction is preamplifier noise, σ_{amp}. For charge-integrating preamplifiers with negligible input current noise, the following expression correctly describes the behavior of the noise:
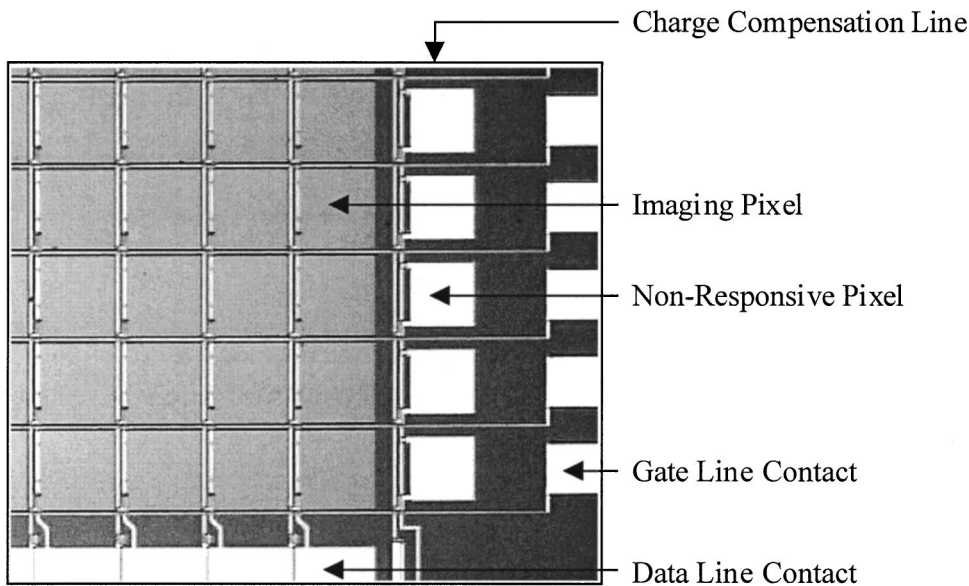
FIG. 3. Microphotograph of a corner of an indirect detection array whose design includes a compensation line. The construction of the compensation line pixels is equivalent to that of normal pixels other than for the presence of a layer of opaque material over the photodiode that blocks the light. This array, with a 508 μm pitch and 512 ×512 pixels, was developed for radiotherapy applications (Ref. 18).

$$\sigma_{amp} = \sigma_{base} + \delta C_{in}. \tag{5}$$

In Eq. (5) σ_{base} and δ are the base noise and noise slope of the preamplifier, respectively, and C_{in} is the magnitude of the input capacitance of the data line. Preamplifier noise reduction could result from improved array design which lowers C_{in} as well as improved preamplifier design which diminishes σ_{base} and δ. For present array designs, the data line capacitance mainly originates from two approximately equally-contributing sources: parasitic capacitance arising from overlap of the gate and source contacts in the pixel TFTs, and from the crossover of the data and gate lines.[6] As a result, the minimum capacitance per pixel for current state-of-the-art arrays is ~24.4 fF/pixel.[2] However, through the incorporation of self-aligned pixel TFTs (Ref. 21) (which have no gate–source overlap and thus exhibit negligible parasitic capacitance) and through the adoption of thicker, low-dielectric-constant passivation layers (which would greatly reduce crossover capacitance), an overall reduction of 90% in C_{in} should be possible in the future. Preamplifier noise could also be reduced through improved preamplifier design, although this can only be accomplished with proper attention to various considerations relating to operating conditions and design. For example, to reduce noise the design of the preamplifier must be tailored to the magnitude of the anticipated input capacitance and the bandwidth of the circuit must be minimized, since noise generally increases with the square root of the bandwidth. However, the time constant of the circuit (which is inversely proportional to the bandwidth) must also be sufficiently short to allow readout of the array at the desired rate (e.g., 30 fps). An example of a relatively low noise chip, designed with regard to such considerations, is a 128-channel preamplifier-multiplexer prototype recently created by our group for fluoroscopic-radiographic AMFPI research (based on an earlier 32-channel device[22]). This prototype has demonstrated a base noise of ~110 e [rms] and a noise slope of ~8e/pF. Given the possibilities of reduced data line capacitance and improved preamplifier

performance, it is anticipated that values for σ_{amp} of ~150 e [rms] and ~130 e [rms] can be achieved for 20 cm arrays (corresponding to a dimension being pursued by various groups interested in fluoroscopy[7,14,16]) with pixel pitches of 100 μm and 200 μm, respectively.

As other additive noise sources are reduced, external line noise ($\sigma_{ext-line}$), which originates from sources beyond the array, such as acquisition system power supplies, will continue to pose a challenge. Due to the previously mentioned capacitive coupling in the arrays, power supply noise couples to all data lines simultaneously creating a significant noise component. Consequently, when preamplifiers sample the analog pixel signals along a given gate line, they also sample the combined effect of power supply noise coupled to that data line from all the other gate lines. Thus the noise from even the quietest power supplies is magnified by the number of rows of pixels in an array design.[23] Moreover, by virtue of how it is created, this noise component exhibits a high degree of correlation between different data lines. A common method for suppressing line noise is through the use of custom-designed preamplifiers containing dual-correlated sampling circuitry.[20,22] Such circuits sample signal from the data line twice; typically prior to the period when the pixel TFTs along the selected gate line are conducting, and during this interval. These two samples are then subtracted before digitization in order to cancel common noise components. While in principle effective for eliminating noise components whose temporal variation is slow compared to the two sampling intervals (i.e., lower frequency components), this technique does not remove higher frequency components of the line noise.

A strategy that offers the possibility of completely eliminating the correlated component of external line noise involves using the line noise measured from one data line as the basis of a correction for pixels along other lines. A means of exploiting this principle involves the incorporation of multiple columns (i.e., data lines) of nonresponsive pixels
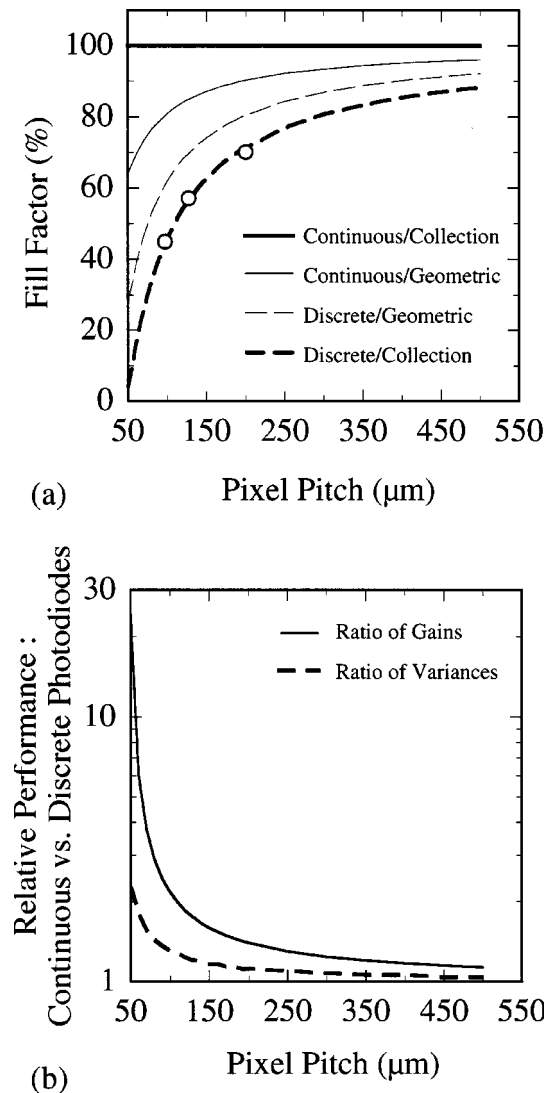
TABLE II. Selected properties of two scintillators, CsI(Tl) and Gd$_2$O$_2$S:Tb, used in indirect x-ray detection as well as those of two photoconductors, a-Se and PbI$_2$, used in direct x-ray detection (Refs. 20, 30–32, 43–45). The properties listed are the density, ρ, the atomic number, Z, the mean x-ray energy required to produce each optical photon (indirect detection) or electron–hole pair (direct detection), $W_\pm$, and the product of the drift mobility and the lifetime (or trapping time), $\mu\tau$.

X-ray converter	Detection	ρ (g/cm^3)	Z	$W_\pm$ (eV)	$\mu\tau$ (cm^2/V)
CsI(Tl)	Indirect	4.5	55, 53	16	n/a
Gd$_2$O$_2$S:Tb	Indirect	7.3	64, 8, 16	31	n/a
a-Se	Direct	4.3	34	50	1.4×10^{-7}
PbI$_2$	Direct	5.5	82, 53	5–10	1×10^{-6}

FIG. 4. (a) Geometric and optical collection fill factors (thin and thick lines, respectively), plotted as a function of pixel-to-pixel pitch. Results are shown for continuous and discrete photodiode indirect detection arrays (solid and dashed lines, respectively). These estimates and calculations correspond to achievable array design rules and existing knowledge of the behavior of continuous photodiode structures (Ref. 25). Optical collection fill factors for three reported AMFPI arrays incorporating discrete photodiodes (Refs. 2 and 39) are indicated by open circles. (b) System gain for continuous photodiode array designs divided by that for discrete photodiode array designs (solid line). Square of the TFT thermal noise for continuous photodiode array designs divided by that for discrete photodiode array designs (dashed line). Both ratios are plotted as a function of pixel pitch. These curves derive from the values shown in (a).

(which we shall refer to as compensation lines) into the layout of an array. The design of the nonresponsive pixels is identical to that of normal pixels except for the fact that they are made to be insensitive to the incident radiation and thus produce no imaging signal. For example, pixels could be made nonresponsive by shielding them from the incident radiation. Alternatively for indirect detection, the pixel photodiodes could be shielded from incident light. Figure 3 illustrates an example of an indirect detection array with a single compensation line. As in the case of the dual correlated sampling technique, for a given row of pixels the signal from a compensation line pixel would be subtracted (digitally or prior to digitization) from that for each normal pixel along the row. While this subtraction will remove the correlated noise component, the noncorrelated noise of the resulting signal will be greater than for the uncorrected signal since the noncorrelated noise of the normal and nonresponsive pixels (originating, for example, from preamplifier and the TFT thermal noise) will add in quadrature. This magnification of noncorrelated noise can be greatly suppressed through the incorporation of multiple (for example, 64) compensation lines onto the edge of the array. By subtracting an average value (derived from all the compensation lines) from the normal pixel signals, the contribution of uncorrelated noise from the compensation line pixels will be significantly reduced. Furthermore, adjustment for possible variations in the correlated noise along the length of the gate lines could be accomplished by incorporating multiple compensation lines at both sides of the array and using a combination of information from both sets of compensation lines as the basis of a position-dependent correction.

B. Enhancement of system gain

A variety of strategies for increasing system gain are conceivable. For indirect detection AMFPIs, replacing the discrete photodiodes used in present AMFPIs with a continuous photodiode surface would lead to an increase in the optical collection fill factor of the photodiode, a strategy that would be particularly advantageous for high resolution array designs.[24] Recent experiments with small test arrays indicate that the incorporation into each pixel of a discrete structure consisting of an electrical contact coated with n-doped a-Si:H followed by a continuous coating of i-doped and p-doped a-Si:H give good optical efficiency while maintaining a very high degree of isolation between adjacent pixels.[25] These studies strongly support the feasibility of the continuous photodiode approach and further suggest that the resulting optical fill factor may be 100%. For this continuous photodiode array design, the geometric fill factor corresponds to the area of the bottom contact. Maximizing the geometric fill factor helps to maximize the optical fill factor and, for reasons relating to the array fabrication process, the geometric fill factor can be made larger for a continuous photodiode design than for a discrete photodiode design. Consequently, C_{storage} (and $\sigma_{\text{TFT-thermal}}$) for a continuous photodiode array

will be greater than for a discrete photodiode array but less than that corresponding to the full area of the pixel. Realistic upper limits for the magnitude of the geometric and optical fill factors for continuous and discrete photodiode arrays, plotted as a function of pixel pitch, are illustrated in Fig. 4(a). Figure 4(b) shows the corresponding increases in system gain and $\sigma^2_{\text{TFT-thermal}}$ for arrays incorporating continuous photodiodes relative to those with discrete photodiodes. Generally, the enhancement in gain (e.g., ~220% at 100 μm pitch and ~40% at 200 μm pitch) far surpasses the increase in $\sigma^2_{\text{TFT-thermal}}$, particularly for smaller pixels. Therefore, maximizing the optical fill factor is consistent with minimizing the ratio of σ^2_{add} to $\overline{g}_1\overline{g}_k\overline{g}_4 f_{\text{coll}}$.

A second strategy to enhance the system gain would be to incorporate a structure into each pixel that would amplify the signal generated by the incident radiation. Conceivably, this strategy could be pursued in at least two ways; (a) substitution of the photodiode with an avalanche photodiode (APD) or (b) incorporation of a discrete amplifier circuit into each pixel of an indirect or direct detection array. While small area APDs have been developed for many applications, they are generally difficult to fabricate and the prospects of compatibility with large area fabrication in the foreseeable future are uncertain. However, a number of developments in thin-film, flat-panel technologies make the prospects of implementing the second option a definite possibility in the future. In particular, the large and growing interest in thin-film, polycrystalline silicon (poly-Si) for flat-panel electronics is an important development. Poly-Si TFTs have a field-effect mobility 10–100 times larger than that for *a*-Si:H TFTs. While higher mobility makes poly-Si TFTs inferior candidates for pixel switches due to their resulting higher leakage currents, it strongly favors their use for other circuits such as pixel amplifiers and multiplexers for flat-panel imagers and displays.[2,3,26,27] In addition, while a simple common-source amplifier formed from a single TFT can provide gain on the order of times 10, charge integrating amplifiers require more transistors, ~10 probably being sufficient. Early empirical studies using a prototype amplifier design have been encouraging[27] and an initial theoretical analysis of the concept has been reported.[28] Of course, the incorporation of pixel amplifiers would significantly increase the number of TFTs on an array (perhaps by order of magnitude). However, on-going reductions in the minimum feature size in array design, which affects the size of the transistors and which has been partially responsible for the exponential growth in the number of transistors per array over the last decade,[2] can reasonably be expected to continue thereby making the required higher densities of TFTs highly likely in the future.

An alternative approach to significantly increasing system gain would involve the utilization of an x-ray converting material offering a higher sensitivity (i.e., a larger number of secondary quanta per interacting x ray), and thus a higher gain than phosphors, CsI(Tl), or *a*-Se. While a wide variety of candidate radiation detection materials exist, including TlBr, HgI$_2$, CdTe, and CdZnTe,[8,29] one particularly promising material which has recently been under considerable investigation for use in active matrix imagers is lead iodide,
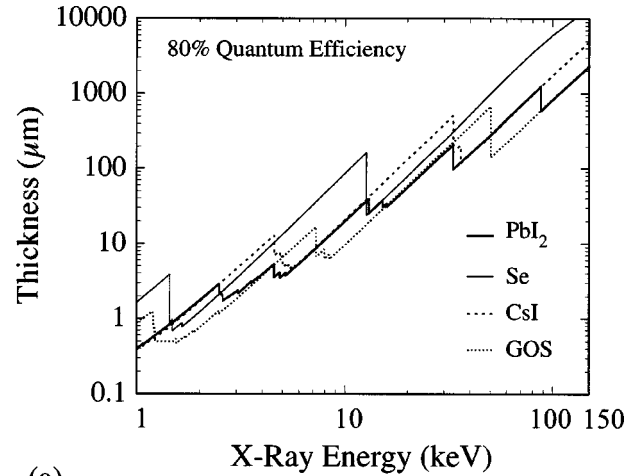
(a)
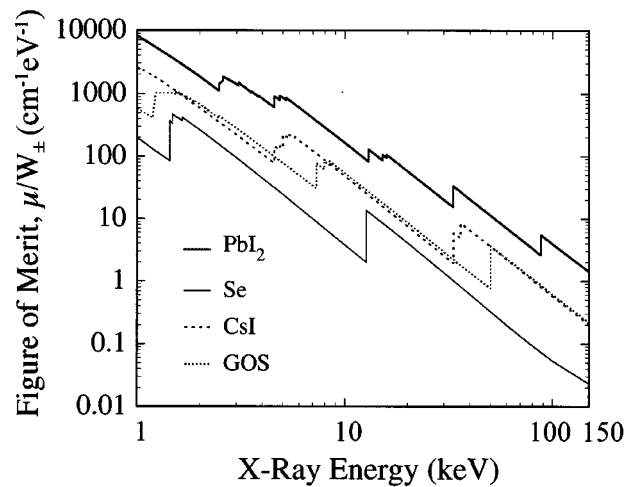
(b)

FIG. 5. Logarithmic plots as a function of monoenergetic x-ray energy of various parameters relating to the four converter materials listed in Table II. (a) Thickness of material required to absorb 80% of incident x rays based on total mass attenuation coefficients given in Ref. 42. (b) Linear x-ray attenuation coefficient divided by the average energy, $W_{\pm}$, required to create each optical photon (for indirect conversion materials) or required to create each *e*-hole pair (for direct detection materials). In (b), a value of 5 eV for $W_{\pm}$ for PbI$_2$ was assumed.

PbI$_2$.[8,30–32] Table II contains a comparison of properties for PbI$_2$ with those for other detection materials which are already used in AMFPI devices. As detailed in Ref. 32, the properties of PbI$_2$ already appear to satisfy most basic requirements[33] for use in a direct detection AMFPI. These include (a) a relatively small value for the average x-ray energy required to create an electron–hole pair, $W_{\pm}$; (b) a product of the drift mobility, μ, lifetime, τ, and applied electric field sufficiently large that the charge carriers can successfully transit thick detection layers; (c) a high atomic number, Z, giving a large absorption coefficient; (d) a high density, ρ, contributing toward good x-ray absorption; (e) process compatibility with active matrix devices permitting deposition of films sufficiently thick for high absorption efficiency; and (f) good spatial resolution. Although the magnitude of the dark current of PbI$_2$ films remains a concern

and is an area of active research, for the purposes of this paper we assume that dark current and the associated shot noise are not performance-limiting factors. This is consistent with the assumptions stated at the beginning of Sec. III A.

Comparisons of some of the properties of CsI(T1), Gd_2O_2S:Tb, *a*-Se, and PbI_2, plotted as a function of monoenergetic x-ray energy, are shown in Figs. 5(a) and 5(b). Figure 5(a) illustrates calculations of the thickness of material required to absorb 80% of the incident x rays. These calculations indicate that, particularly for x-ray converters containing high atomic number constituents, ∼500 to ∼1000 μm of material is sufficient to absorb ∼80% of the incident radiation over much of the energy range that corresponds to normal fluoroscopic and radiographic operating conditions. Moreover, of particular interest in the present context is the fact that the average x-ray energy required to create an electron–hole pair with PbI_2 is ∼5 to 10 times less than that for *a*-Se and ∼3 to 6 times less than that for CsI(Tl) and Gd_2O_2S:Tb. Figure 5(b) illustrates a figure of merit related to system gain consisting of the linear x-ray attenuation coeffi-

cient divided by $W_\pm$. The results are illustrative of the potential of PbI_2 and help to explain the motivation to develop this material for imaging.

IV. METHODOLOGY FOR THEORETICAL EXAMINATION OF IMPROVING AMFPI PERFORMANCE

In order to quantify the effects of implementing additive noise reduction and gain enhancement strategies such as those outlined in the preceding section, a theoretical investigation of the effects on the DQE was performed. These calculations were performed within the cascaded systems formalism discussed in Sec. II B. Calculations of DQE at zero spatial frequency for both indirect and direct detection configurations were performed using Eq. (2). While Eq. (2) does not explicitly account for the effect of noise power aliasing,[34] the following expressions do account for this effect and were also used to calculate DQE at zero as well as nonzero spatial frequencies for indirect and direct detection AMFPIs:

$$\text{DQE}(u,v) = \frac{\bar{g}_1 \bar{g}_2 \bar{g}_4 T_3^2(u,v) T_5^2(u,v)}{\left[1 + \bar{g}_4(\bar{g}_2 + \varepsilon_{g2}) T_3^2(u,v)\right] T_5^2(u,v) ** \dfrac{III(u,v)}{a_{\text{coll}}^4 \bar{q}_0 \bar{g}_1 \bar{g}_2 \bar{g}_4} + \dfrac{S_{\text{add}}(u,v)}{a_{\text{coll}}^4 \bar{q}_0 \bar{g}_1 \bar{g}_2 \bar{g}_4}} \quad \text{indirect,} \tag{6a}$$

$$\text{DQE}(u,v) = \frac{\bar{g}_1 \bar{g}_3 \bar{g}_4 T_2^2(u,v) T_5^2(u,v)}{\left[1 + \bar{g}_4(\bar{g}_3 + \varepsilon_{g3})\right] T_5^2(u,v) ** \dfrac{III(u,v)}{a_{\text{coll}}^4 \bar{q}_0 \bar{g}_1 \bar{g}_3 \bar{g}_4} + \dfrac{S_{\text{add}}(u,v)}{a_{\text{coll}}^4 \bar{q}_0 \bar{g}_1 \bar{g}_3 \bar{g}_4}} \quad \text{direct.} \tag{6b}$$

As before, the conventions for the symbols are as given in Table I and $S_{\text{add}}(u,v)$ corresponds to the noise power spectrum (NPS) of the total additive noise. In addition,

$$III(u,v) = \sum_{k,l=-\infty}^{\infty} \delta(u - ku_s, v - lv_s), \tag{7}$$

where u_s and v_s correspond to sampling frequencies given by

$$u_s, v_s = \frac{1}{a_{\text{pix}}} \tag{8}$$

and a_{pix} is the pixel-to-pixel pitch of the array. Note that Eqs. (6a) and (6b) simplify to the presampling expression given by Eq. (2) for the case of zero spatial frequency and no aliasing since the additive noise power viewed from the presampling stage is $a_{\text{coll}}^2 \sigma_{\text{add}}^2 T_5^2$ (which, upon sampling, gives additive white noise power, $S_{\text{add}}(u,v)$, as expected).

Calculations were performed for a variety of hypothetical indirect and direct detection AMFPI designs representative both of the current state of the technology (conventional designs) as well as designs incorporating the strategies discussed in Sec. III (advanced designs). All designs incorpo-

rated 20 cm long data lines and 500 μm thick indirect [CsI(Tl)] and direct (*a*-Se and PbI_2) detection converters. The choice of converter thickness was governed by the desire to use the largest value for which model parameters could be determined with reasonable confidence, based on published sources as well as our own experience. (Although the 1000 μm *a*-Se calculation shown in Fig. 1 does not fully satisfy this criteria, the model parameters are sufficiently well understood to allow a specific, limited point, to be made.) Calculations were performed both under fluoroscopic conditions at 80 kVp and radiographic conditions at 110 kVp. The x-ray spectra, derived from Ref. 35, were based on a 17° tungsten target, an aluminum filtration of ∼3 mm, and an air path of 75 cm. Based on the methodology of Ref. 12, the mean x-ray fluence incident upon the imager per unit exposure was calculated to be 1.98×10^5 and 2.30×10^5 x rays mm^2/mR for the 80 and 110 kVp spectra, respectively.

For all calculations, values for the quantum detection efficiency of the converter ($\bar{g}_1$) were derived from information given in Ref. 36. The quantum gain for the indirect and direct detection converters ($\bar{g}_2$ and $\bar{g}_3$, respectively) were based on the values of $W_\pm$ given in Table II. (For PbI_2, the

TABLE III. Values of various parameters used in the cascaded systems calculations. These parameters correspond to 500 μm of each of the specified x-ray detection materials at the indicated energies. Note that the subscript k represents stage 2 or stage 3 for indirect or direct detection, respectively.

	CsI(Tl)		*a*-Se		PbI$_2$	
Parameters	80 kVp	110 kVp	80 kVp	110 kVp	80 kVp	110 kVp
$\bar{g}_1$	0.92	0.84	0.72	0.58	0.94	0.87
$\bar{g}_k$	1690	2000	770	890	8220	9720
ϵ_{g_k}	370	490	80	110	920	1330

value at the low end of the range, 5 eV, was assumed.) The determination of the quantum gain and Swank noise[37] involved a finite-element analysis technique[37,38] in order to account for the depth of x-ray interactions as well as k-fluorescence x-ray production, emission, and reabsorption. In addition, the determination of $\bar{g}_2$ for CsI(Tl) assumed a top white reflector [which was assumed to reflect all of the light but which exhibits degraded modulation transfer function (MTF) Ref. 20] and an optical photon escape efficiency of 80%.[20] Values for the Poisson excess (ε_{g2} and ε_{g3}) for each converter were determined from the corresponding values of quantum gain and Swank noise. The numerical values used in the calculations for these parameters are summarized in Table III.

For indirect detection, calculations were performed for discrete photodiode arrays (conventional AMFPIs) and for continuous photodiode arrays (advanced AMFPIs). For both the discrete and continuous photodiode calculations, the optical collection fill factors (to which a_{coll}^2 corresponds) were obtained from the appropriate curves in Fig. 4(a). The coupling efficiency ($\bar{g}_4$) for all indirect detection calculations, obtained from the spectral sensitivity of the photodiodes[6] and the spectral output of CsI(Tl), was determined to be 0.65.

For direct detection calculations, the values used for a_{coll}^2 (and hence the collection fill factor) depended on the photoconductor. For *a*-Se, a_{coll}^2 was assumed to correspond to the area of the collection electrode. For direct detection array designs, this area corresponds to the geometric fill factors for continuous photodiode arrays given in Fig. 4(a). In the case of PbI$_2$, a_{coll}^2 was assumed to be given by a_{pix}^2 as this is strongly suggested by early studies involving test arrays by the authors—a result most likely due to the relatively higher photoconductivity of the material. For both photoconductors, the collection efficiency ($\bar{g}_4$, which relates to how efficiently electron–hole pairs are extracted from the photoconductor volume corresponding to the collection fill factor) was assumed to be unity.

For all calculations, T_5 was determined from the since function associated with the area corresponding to the collection fill factor. For the indirect detection calculations, T_3 was obtained from published measurements of the presampled MTF for CsI(Tl).[7,39] For direct detection calculations, T_2 is assumed to be unity for both *a*-Se (Ref. 10) and PbI$_2$.

Calculations for conventional AMFPI designs were performed only at 200 μm pitch with CsI(Tl) and *a*-Se. In these calculations, a total additive noise (σ_{add}) of 1200 e [rms] is

assumed.[39] Calculations for advanced AMFPI designs were performed at 100 and 200 μm pitch with CsI(Tl), *a*-Se, and PbI$_2$. Calculations were also performed for advanced CsI(Tl) and *a*-Se designs that incorporated a pixel amplifier. (None of the PbI$_2$ calculations included the assumption of a pixel amplifier.) For the pixel amplifier calculations, the noise contribution from the amplifier[28] was assumed to be zero. To account for the presence of this amplifier in the cascaded systems model, a gain stage is added between stages 5 and 6. After simplification, the resulting effect upon the previous expressions for DQE is to multiply the factors $a_{\mathrm{coll}}^2\bar{q}_0\bar{g}_1\bar{g}_k\bar{g}_4$ in Eq. (2) and $a_{\mathrm{coll}}^4\bar{q}_0\bar{g}_1\bar{g}_k\bar{g}_4$ in Eqs. (6a) and (6b) by a factor representing the square of the gain of the amplifier.

The magnitude of the additive noise for the advanced AMFPI calculations was based upon the following considerations and assumptions. Consistent with Sec. III A, contributions from shot noise, flicker noise, and ADC noise are assumed to be negligible, although the effect of additional additive noise from these sources as well as from the pixel amplifier was also explored. It is also assumed that the external line noise contains no uncorrelated components and that the correlated components can be completely suppressed through the combined use of dual correlated sampling and compensation lines, as previously discussed. In addition, the magnitude of σ_{amp} for an array with 20 cm long data lines is assumed to be 150 and 130 e [rms] for 100 and 200 μm pitch arrays, respectively, following the preamplifier noise-reduction discussion of Sec. III A. Finally, the magnitude of the TFT thermal noise, as computed using Eq. (4), was minimized through selection of C_{storage} according to the following considerations. For all designs, the signal capacity of the pixels, Q_{max} [given by Eq. (1), assuming a magnitude for V_{storage} of 10 V] must be able to accommodate a large radiographic irradiation, taken to be a 3 mR exposure at 120 kVp. Specifically, for indirect detection designs this maximum signal was not allowed to exceed 90% of the total charge storage capacity of the pixel so as to maintain a highly linear signal response. In addition, for both discrete and continuous photodiodes, given that the area of the storage capacitor corresponds to the geometric fill factor [Fig. 4(a)], the maximum signal size was accommodated through adjustment of the photodiode thickness, with a maximum thickness of 3 μm (as per the discussion in Sec. III A). In the case of direct detection designs, the maximum signal may be up to 100% of the capacity of the pixel. The resulting values for the total additive noise used in the calculations are given in Table IV.

Given that imager designs capable of both radiographic and fluoroscopic operation are possible with AMFPI technology, it is interesting to examine the performance of devices capable of high resolution readout, specifically those with $\sim$100 μm pixel pitch.[2] Such devices would be capable of providing high quality radiographic images when operated at full resolution (100 μm; corresponding to 1×1 pixel readout). In addition, these devices could also be operated in fluoroscopic mode at various resolutions; full resolution, half-resolution (200 μm; corresponding to 2×2 pixel readout), etc. While variable resolutions could be achieved by

TABLE IV. Values of the total additive noise, σ_{add}, used in the DQE calculations for the various hypothetical advanced AMFPI designs at pixel pitches of 100 μm and 200 μm. Results are shown for indirect detection AMFPIs using CsI(Tl) and direct detection AMFPIs using a-Se and PbI$_2$. Results are also shown for CsI(Tl) and a-Se designs which include a pixel amplifier providing a further factor of 10 gain. Note while these values correspond to an array with 20 cm data lines, they remain almost unchanged for an array with 40 cm data lines.

X-ray converter	σ_{add} for 100 μm pitch e [rms]	σ_{add} for 200 μm pitch e [rms]
CsI(Tl)	340	650
CsI(Tl) with $\times 10$ gain	490	1320
a-Se	190	280
a-Se with $\times 10$ gain	410	810
PbI$_2$	570	1110

digitally summing pixels acquired at full resolution, an alternative method[6] involves reading out pairs (or triples, etc.) of consecutive gate lines at a time so as to automatically sum the signals for pairs (or triples, etc.) of pixels along a data line. (Summation of pixels along the gate line direction could conveniently be done digitally at a later stage.) Thus, an acquisition system capable of 30 fps readout of the full area of an array at only 200 μm resolution (by simultaneous readout of pairs of gate lines) could be used to acquire image frames from a smaller area at 100 μm pitch at the same frame rate—a form of digital zoom. Alternatively, the same acquisition system could be used to read out a given region of an array at progressively higher frame rates (consistent with the pixel time constants[40]) at correspondingly lower levels of resolution. Calculations were performed for 100 μm pixel pitch AMFPI designs both at full resolution and half-resolution. The half-resolution calculations correspond to simultaneous readout of a pair of gate lines and digital summation of signals from adjacent data lines. This involved linear combinations of pixel signals and of variances associated with x-ray quanta. It also involved an increase by a factor of 2 in the TFT thermal noise ($\sigma_{\text{TFT-thermal}}$), and an increase by the square root of 2 in the external preamplifier noise (σ_{amp}).

V. RESULTS

The effects of variations in system gain, $\bar{g}_1 \bar{g}_k \bar{g}_4 f_{coll}$, and total additive noise, σ_{add}, on AMFPI performance are quantitatively examined in Figs. 6(a), 6(b), and 6(c). The calculations shown correspond to 200 μm pixel pitch AMFPI designs. Figure 6(a) shows DQE(0) calculations for a conventional CsI(Tl) AMFPI design as a function of increasing gain, assumed to be due to the incorporation of a pixel amplifier. Calculations are shown at exposures representative of lower, average, and upper values for fluoroscopy. As in Fig. 2, these calculations again demonstrate that with no gain enhancement (corresponding to unity on the horizontal axis) there is a significant reduction in DQE(0), particularly at lower exposures. However, as the gain increases, the DQE(0) increases toward its asymptotic limit with a factor of 10 enhancement sufficient to reach or closely approach this limit,

even at the lowest exposure. Similarly, a factor of 10 enhancement also allows the DQE(0) to closely approach the asymptotic limit in the case of a conventional a-SeAMFPI design, as illustrated in Fig. 6(b).

Figure 6(c) shows DQE(0) calculations for conventional [CsI(Tl) and a-Se] and advanced (PbI$_2$)AMFPI designs as a function of total additive noise, at an average fluoroscopic exposure. In addition, calculations assuming a factor of 10 gain enhancement due to a pixel amplifier are also shown for CsI(Tl) and a-Se. (Henceforth, calculations corresponding to the incorporation of a pixel amplifier in the array design will always assume an additional factor of 10 increase in gain due to the amplifier.) In the case of the conventional CsI(Tl) and a-Se designs there is a steady increase in DQE(0) with diminishing σ_{add}, almost down to zero additive noise. However, in the case of the CsI(Tl) and a-Se designs with a pixel amplifier as well as the PbI$_2$ design, the effect of decreasing σ_{add} is considerably less. Although the importance of minimizing additive noise increases at lower exposures (and higher spatial frequencies) for all of these designs, those designs with a factor of 10 gain from a pixel amplifier and with PbI$_2$ always exhibit a comparatively weaker dependence on additive noise.

A comparison of DQE(0) performance as a function of exposure for conventional and advanced 200 μm pitch AMFPI designs, including advanced CsI(Tl) and a-Se designs with and without a pixel amplifier, is shown in Fig. 7. Compared to the performance of the conventional designs, the reduced total additive noise of the advanced CsI(Tl) and a-Se designs without a pixel amplifier [aided to a limited extent by the improved optical collection fill factor in the case of the advanced CsI(Tl) design] significantly reduces the falloff in DQE(0) with decreasing exposure resulting in performance improvements as large as $\sim 40\%$. Moreover, the very high gain designs [i.e., the advanced CsI(Tl) and a-Se designs with a pixel amplifier and the advanced PbI$_2$ design] all exhibit a high DQE(0) (limited by the x-ray quantum efficiency and Swank noise of the converter) which is practically independent of exposure.

The effects of adding noise power aliasing[34] to the DQE(0) calculations, compared to calculations without aliasing, are illustrated in Figs. 8(a) and 8(b). In Fig. 8(a), calculations for advanced CsI(Tl) and a-Se AMFPI designs (with and without a pixel amplifier) and calculations for an advanced PbI$_2$ design are presented as a function of exposure. In the case of the CsI(Tl) designs, the DQE(0) calculations with and without aliasing are indistinguishable due to the negligible magnitude of the NPS near the sampling frequency of the system. However, at frequencies approaching the Nyquist frequency (which is equal to one-half of the sampling frequency), the effect of aliasing is to reduce the DQE. This is a consequence of the fact that the NPS is non-negligible at frequencies just beyond the Nyquist frequency. In the case of a-Se, the assumption of a collection fill factor that is less than unity results in a reduction in the DQE(0) due to noise power aliasing.[13] At nonzero frequencies, the reduction of DQE due to aliasing is even greater for a-Se due to the fact that the aliased noise power is nonzero and con-
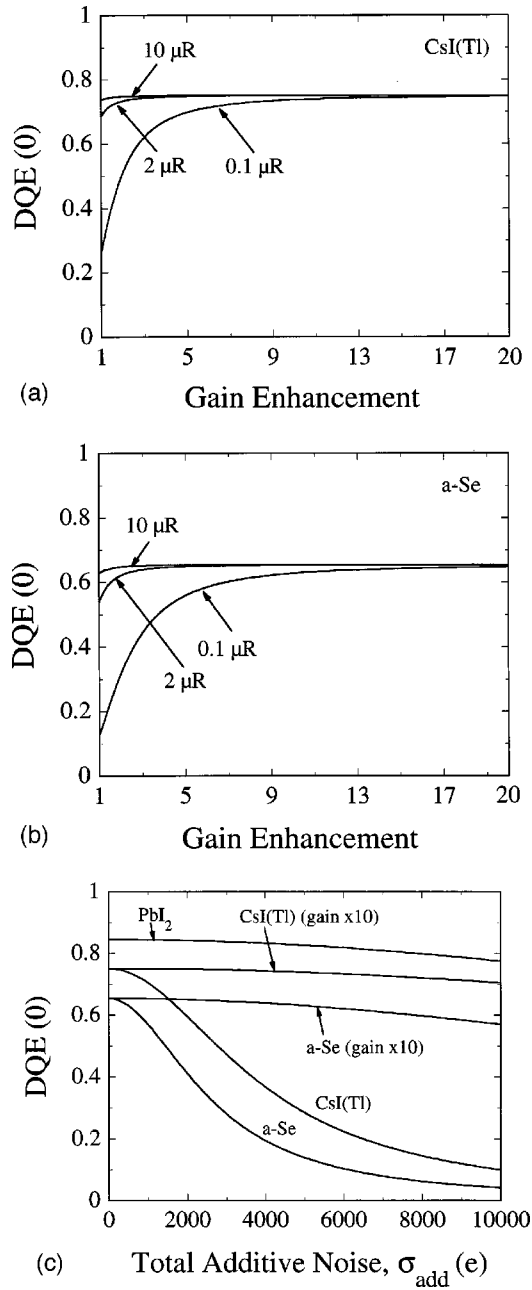
(a)

(b)

(c)

FIG. 6. Plots of zero-frequency DQE, assuming a 200 μm pixel pitch and an energy of 80 kVp, based on Eq. (2). (a,b) Calculations for DQE(0) plotted as a function of the degree of gain enhancement provided by a pixel amplifier. On the horizontal axis, unity corresponds to no additional gain enhancement, 2 corresponds to an enhancement of gain by a factor of 2, and so on. Calculations are shown for three detector exposures spanning the range associated with fluoroscopy. Other than for the gain enhancement due to the pixel amplifier, the parameters assumed in the calculations shown in (a) and (b) correspond to those of conventional CsI(Tl) and a-Se designs, respectively. (c) Calculations at an exposure of 2 μR for various AMFPI designs, plotted as a function of total additive noise. Results are shown for CsI(Tl) and a-Se, both with and without a factor of 10 gain enhancement from a pixel amplifier. Other than for the pixel amplifier and the variation in total additive noise, these calculations assume parameters corresponding to conventional AMFPI designs. Results are also shown for an advanced PbI$_2$ design, assuming variable total additive noise. In this and the following figures, calculations which include the assumption of a pixel amplifier were based on a modified form of Eq. (2) [or a modified form of Eqs. (6a) and (6b)], as described in Sec. IV. In addition, the notation ''(gain ×10)'' is used in the figures to indicate those calculations which include the assumption of a pixel amplifier.

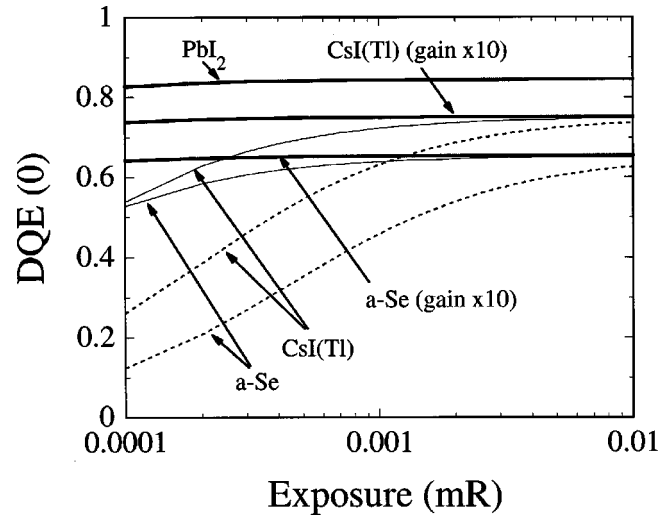
FIG. 7. Plot of zero-frequency DQE as a function of exposure, based on Eq. (2). These calculations assume a 200 μm pixel pitch and an energy of 80 kVp and the exposures correspond to the range associated with fluoroscopy. Calculations are shown for conventional CsI(Tl) and a-Se AMFPI designs (dashed lines) and advanced CsI(Tl) and a-Se designs (thin solid lines). Calculations are also shown for advanced, very high gain designs: CsI(Tl) and a-Se incorporating a pixel amplifier and PbI$_2$ (thick solid lines). In this and all following calculations, the incorporation of the pixel amplifier in a design is assumed to confer an additional factor of 10 gain enhancement.

stant up to the Nyquist frequency.[13] Finally, in the case of the PbI$_2$ design, the DQE(0) calculations with and without noise power aliasing are indistinguishable due to the assumption of unity collection fill factor.[13] At nonzero frequencies, aliasing reduces the DQE for PbI$_2$ for the same reasons as for a-Se.

Figure 8(b) shows zero frequency DQE calculations, with and without noise power aliasing, as a function of collection fill factor. Calculations are shown for advanced CsI(Tl) and a-Se AMFPI designs with a pixel amplifier and an advanced PbI$_2$ design. Results were computed at an average fluoroscopic exposure. In the case of the direct detection (a-Se and PbI$_2$) designs, the effect of noise power aliasing is to multiply calculations that do not include aliasing by the collection fill factor,[13] thereby reducing the DQE(0). In the case of the indirect detection [CsI(Tl)] design, the effect of noise power aliasing is negligible for the same reasons as noted for the Fig. 7 results. The trends seen in these calculations are unchanged for advanced CsI(Tl) and a-Se designs that do not include a pixel amplifier (not shown for reasons of clarity).

Calculations that illustrate the frequency dependence of the DQE for advanced CsI(Tl), a-Se, and PbI$_2$ AMFPI designs are shown in Fig. 9. (These and all further calculations include the effects of noise power aliasing.) The calculations were performed at an average fluoroscopic exposure. In the case of the CsI(Tl) design without a pixel amplifier, there is a significant falloff in DQE at higher spatial frequencies. However, introducing a pixel amplifier results in a substantial increase in the DQE at higher frequencies. In the case of the a-Se designs, the falloff of DQE with spatial frequency is governed by the square of the system MTF. For the exposure used in the calculations, the relative size of the total additive
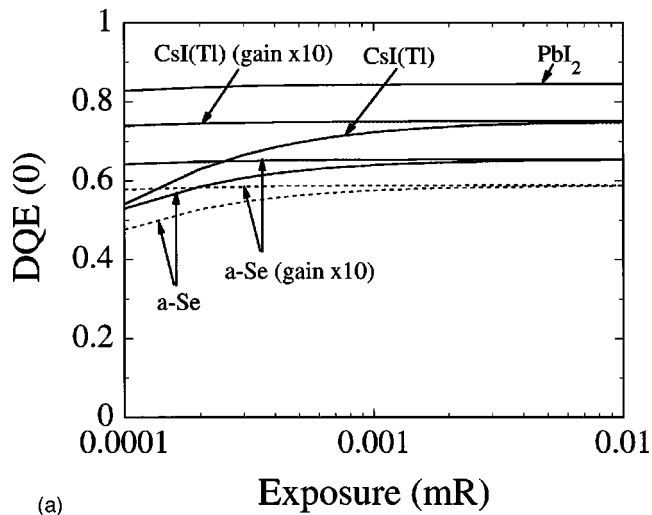
(a)
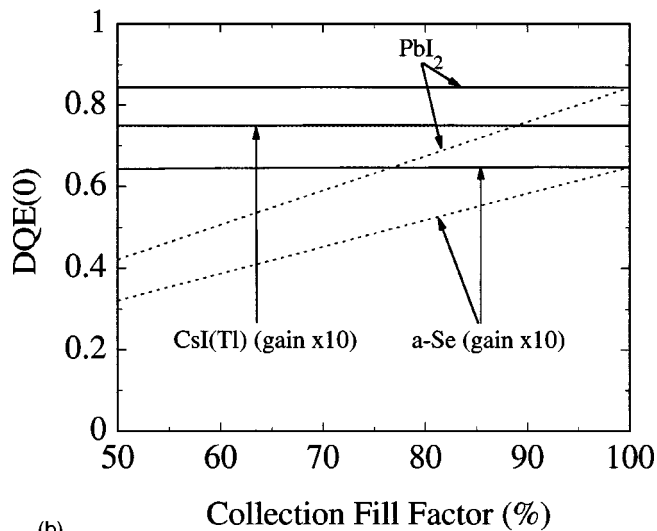
(b)

FIG. 8. Comparison of zero-frequency DQE calculations with and without the inclusion of noise power aliasing, represented by dashed and solid lines, respectively. These calculations assume a pixel pitch of 200 μm and are based on Eqs. (2), (6a), and (6b). (a) Calculations, as a function of exposure across the fluoroscopic range, for advanced CsI(Tl) and *a*-Se AMFPI designs. Results both with and without a pixel amplifier are shown. Calculations are also shown for an advanced PbI$_2$ design. (b) Calculations, as a function of collection fill factor, for advanced CsI(Tl) and *a*-Se designs with a pixel amplifier and for a PbI$_2$ design. In these calculations, for each design the total additive noise has been kept fixed at the corresponding value used in (a).

noise compared to the system gain of the *a*-Se design without a pixel amplifier is such that the introduction of an amplifier results in only small improvement. However at lower exposures (not shown), the incorporation of an amplifier has a progressively larger effect upon the DQE. Finally, at the highest spatial frequencies the calculations suggest that the rate of decline in DQE for the *a*-Se designs is less than that for both CsI(Tl) designs. The behavior of the DQE for the PbI$_2$ design is also governed by the square of the system MTF and, consequently, the shape of the resulting curve is the same as for the *a*-Se designs.

The dependence of DQE on spatial frequency and total additive noise for advanced CsI(Tl) and *a*-Se AMFPI de-
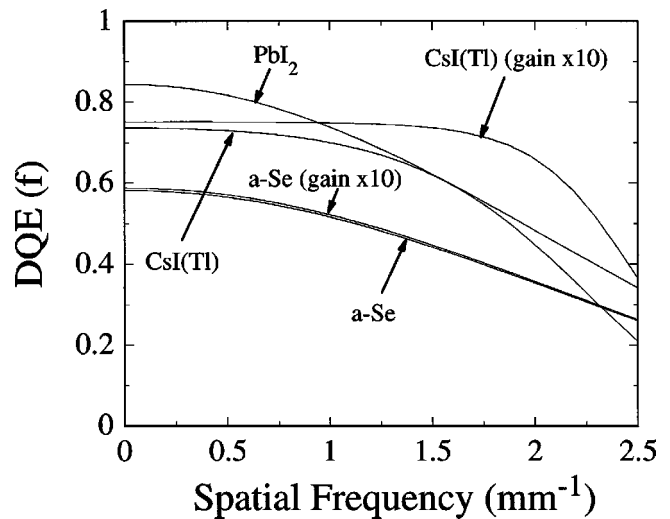

FIG. 9. Plot of DQE as a function of spatial frequency. The calculations assume a pixel pitch of 200 μm, an exposure of 2 μR, and are based on Eqs. (6a) and (6b). Results are shown for advanced CsI(Tl) and *a*-Se AMFPI designs, both with and without a pixel amplifier. Results are also shown for an advanced PbI$_2$ design.

signs with a pixel amplifier and for an advanced PbI$_2$ design is shown in Figs. 10(a), 10(b), and 10(c), respectively. These calculations were performed at an average fluoroscopic exposure. The results indicate that, at this exposure, the DQE exhibits only gradual decline with increasing additive noise. Thus, additional incremental contributions of additive noise from sources beyond those assumed in the present calculations (such as uncorrelated line noise, shot noise, and pixel amplifier noise[28]) should not have a strong, adverse effect on the performance of such very high gain designs. Of course, the effects of incremental additive noise on these designs are larger at lower exposures but remain substantially less than for conventional designs, as previously illustrated in Fig. 6(c).

Figure 11 illustrates DQE(0) calculations for advanced 100 μm pitch AMFPI designs over an exposure range corresponding to fluoroscopy. The calculations were performed for CsI(Tl) and *a*-Se designs with and without a pixel amplifier as well as for a PbI$_2$ design. For each design, calculations are shown for full resolution readout and half-resolution readout, as described in Sec. IV. In the case of the CsI(Tl) and *a*-Se designs without a pixel amplifier, the full resolution mode demonstrates only slightly lower DQE(0) than the half-resolution mode at lower exposures while at higher exposures there is no difference. Furthermore, the differences exhibited by the calculations are much less than for conventional CsI(Tl) and *a*-Se designs (not shown) due to their considerably higher levels of preamplifier and line noise. For the very high gain designs, in all cases there is no difference between full resolution and half-resolution readout. Finally, this figure also illustrates that at sufficiently high exposures, the advantage enjoyed by the very high gain designs disappears, consistent with the discussion following Eq. (2) in Sec. II B.

CsI(Tl) (gain x10)

(a)
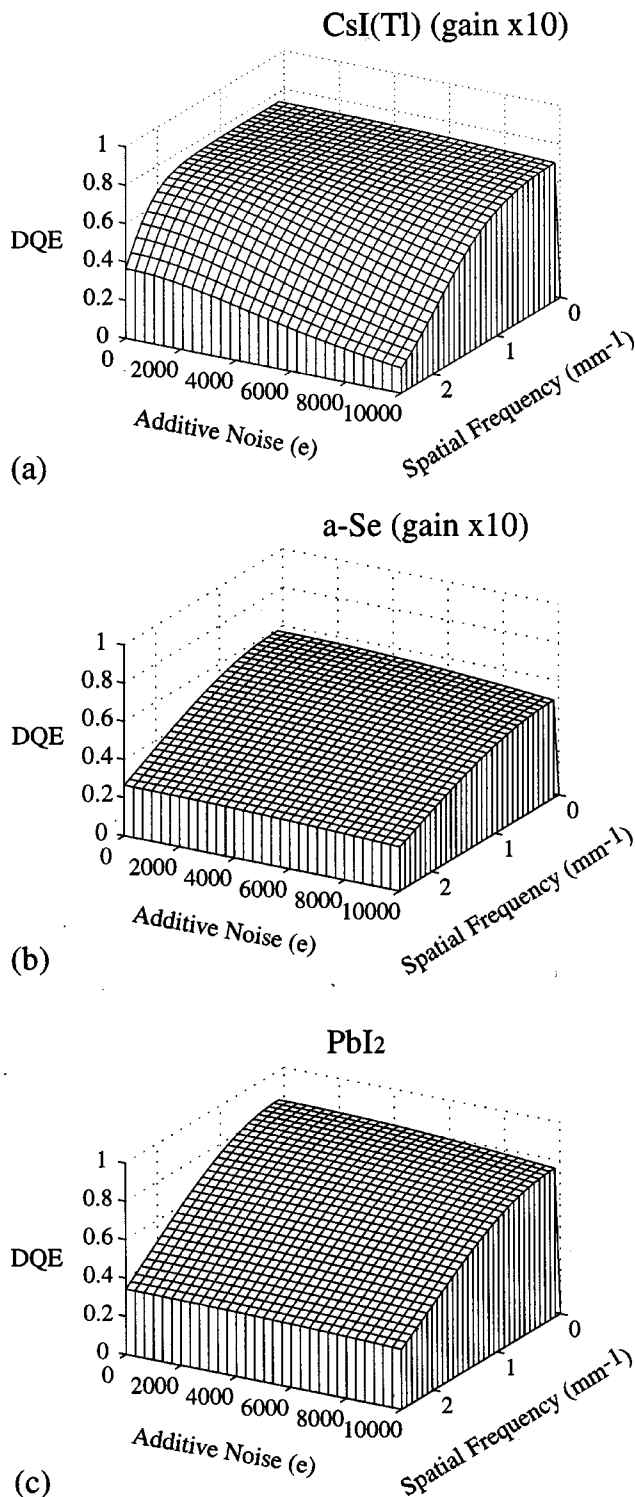
a-Se (gain x10)

(b)

PbI2

(c)

FIG. 10. Plots of DQE as a function of spatial frequency and total additive noise. Other than for the variation in total additive noise, these calculations assume parameters corresponding to (a) an advanced CsI(Tl) AMFPI design and (b) an advanced *a*-Se design, both incorporating a pixel amplifier, and to (c) an advanced PbI$_2$ design. The calculations assume a pixel pitch of 200 μm, an exposure of 2 μR, and are based on Eqs. (6a) and (6b).

The dependence of DQE on spatial frequency and exposure for advanced AMFPI designs having a pixel pitch of 100 μm are shown in Figs. 12 and 13. Calculations were performed for CsI(Tl) and *a*-Se designs incorporating a pixel
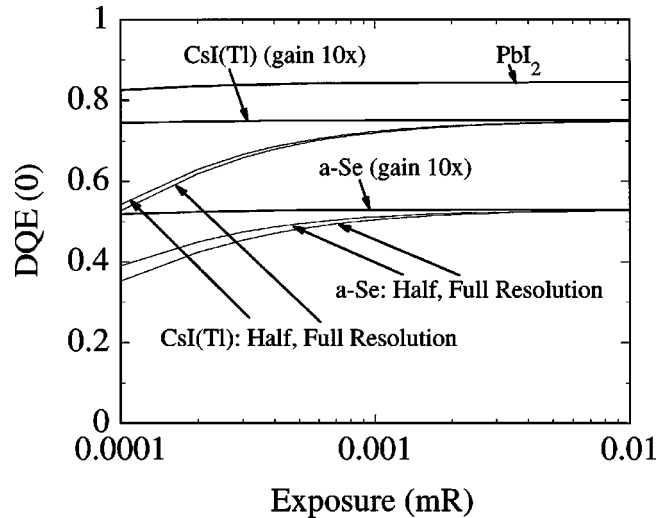

FIG. 11. Plots of zero-frequency DQE as a function of exposure for various 100 μm pixel pitch designs, based on Eqs. (6a) and (6b). The calculations were performed at 80 kVp over an exposure range corresponding to that used for fluoroscopy. The calculations correspond both to full resolution readout (100 μm, corresponding to individual pixel readout) and half-resolution readout (200 μm, corresponding to simultaneous readout of pairs of gate lines). Results are shown for advanced CsI(Tl) and *a*-Se AMFPI designs, both with and without a pixel amplifier. Calculations are also shown for an advanced PbI$_2$ design. The results for full and half-resolution readout are indistinguishable for each of the CsI(Tl) and *a*-Se designs with a pixel amplifier and for the PbI$_2$ design.

amplifier and for a PbI$_2$ design. The calculations appearing in Fig. 12 were performed at 80 kVp over a range of exposures corresponding to fluoroscopy and for spatial frequencies up to the Nyquist limits. Results for full resolution (100 μm) readout up to 5 lp/mm are shown for CsI(Tl), *a*-Se, and PbI$_2$ in Figs. 12(a), 12(b), and 12(c) respectively. Results for half-resolution (200 μm) readout up to 2.5 lp/mm are shown for CsI(Tl), *a*-Se, and PbI$_2$ in Figs. 12(d), 12(e), and 12(f), respectively. For the entire frequency range for the *a*-Se and PbI$_2$ designs and for lower frequencies for the CsI(Tl) design, the DQE is relatively independent of exposure (in sharp contrast to the performance of conventional AMFPI designs[9,13,26]) in both readout modes. In the case of the CsI(Tl) design, the falloff in DQE with increasing frequency is more pronounced for higher frequencies and for full resolution readout. For the *a*-Se and PbI$_2$ designs, the falloff of DQE with increasing frequency, which is primarily governed by the square of the system MTF, is more constant than for CsI(Tl). In addition, the general shape and magnitude of the DQE surfaces for full resolution and half-resolution readout are very similar, relative to the Nyquist frequency limits, for each of the *a*-Se and PbI$_2$ designs.

The calculations appearing in Figs. 13(a), 13(b), and 13(c) correspond to the same readout mode (full resolution), spatial frequency range, and AMFPI designs as for Figs. 12(a), 12(b), and 12(c), respectively, but were performed at 110 kVp over a range of exposures corresponding to radiography. For the CsI(Tl) design, the higher exposure levels of the Fig. 13(a) calculations leads to a reduction in the falloff of DQE with increasing frequency compared to the fluoroscopic cal-
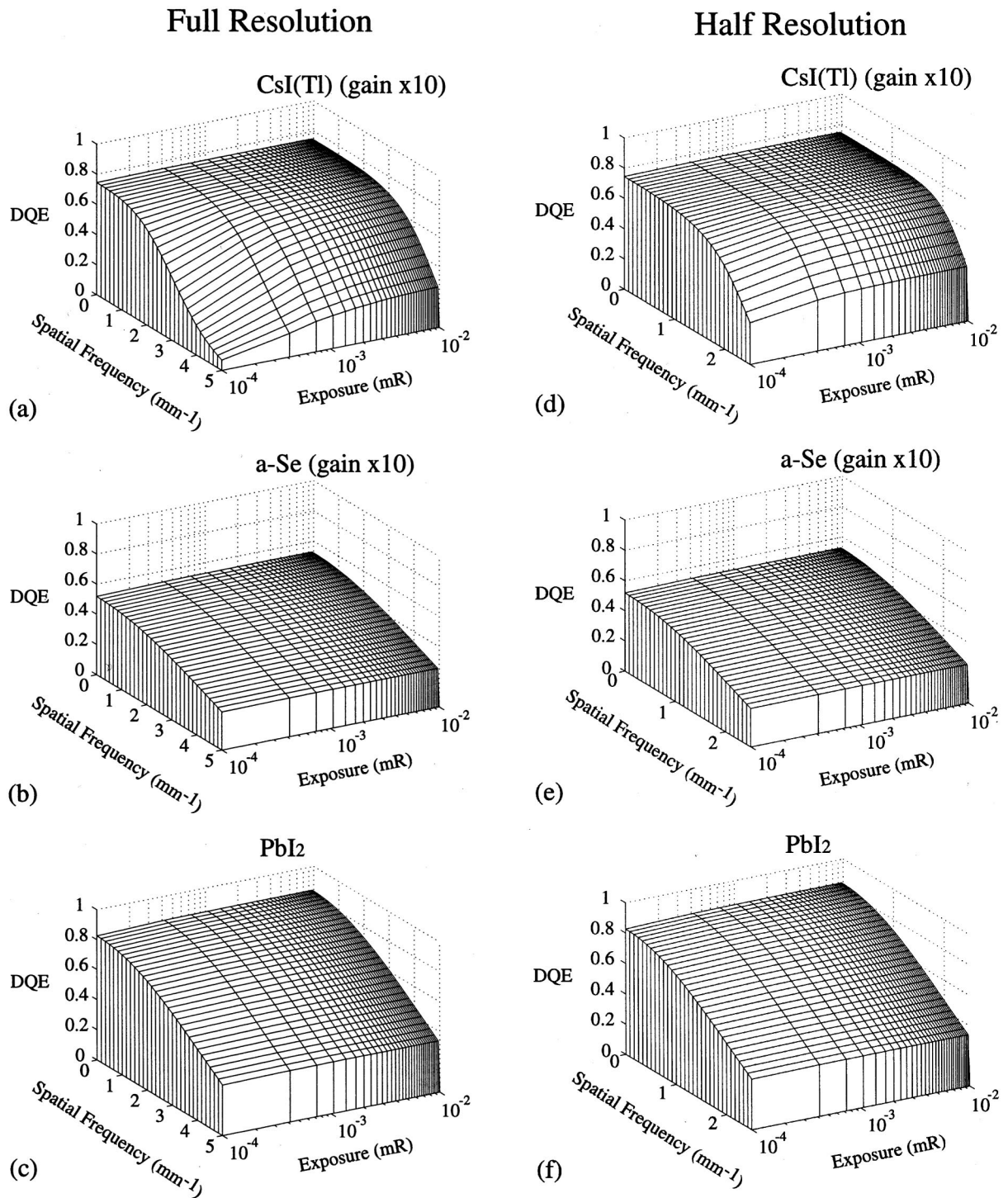
Full Resolution

CsI(Tl) (gain x10)

(a)

a-Se (gain x10)

(b)

PbI₂

(c)

Half Resolution

CsI(Tl) (gain x10)

(d)

a-Se (gain x10)

(e)

PbI₂

(f)

F$_{IG}$. 12. Plot of DQE as a function of spatial frequency and exposure, based on Eqs. (6a) and (6b). The calculations were performed for both full and half-resolution readout at 80 kVp for advanced AMFPI designs with a 100 μm pixel pitch. The range of exposures corresponds to that associated with fluoroscopy while the spatial frequencies extend up to the Nyquist limit (5 lp/mm for full resolution readout, 2.5 lp/mm for half-resolution readout). (a,d) Calculations for a CsI(Tl) design with a pixel amplifier under conditions of full and half-resolution readout, respectively. (b,e) Calculations for an *a*-Se design with a pixel amplifier under conditions of full and half-resolution readout, respectively. (c,f) Calculations for a PbI$_2$ design under conditions of full and half-resolution readout, respectively.

culations of Fig. 12(a). In the case of the *a*-Se and PbI$_2$ designs, the calculations indicate that little difference is to be expected in DQE performance between radiographic and fluoroscopic conditions. (The slight reduction in the maxi-

mum DQE values reported in Fig. 13 compared to those of Fig. 12 is a simple consequence of the use of a higher x-ray energy representative of chest radiography for the radiographic calculations.)

CsI(Tl) (gain x10)
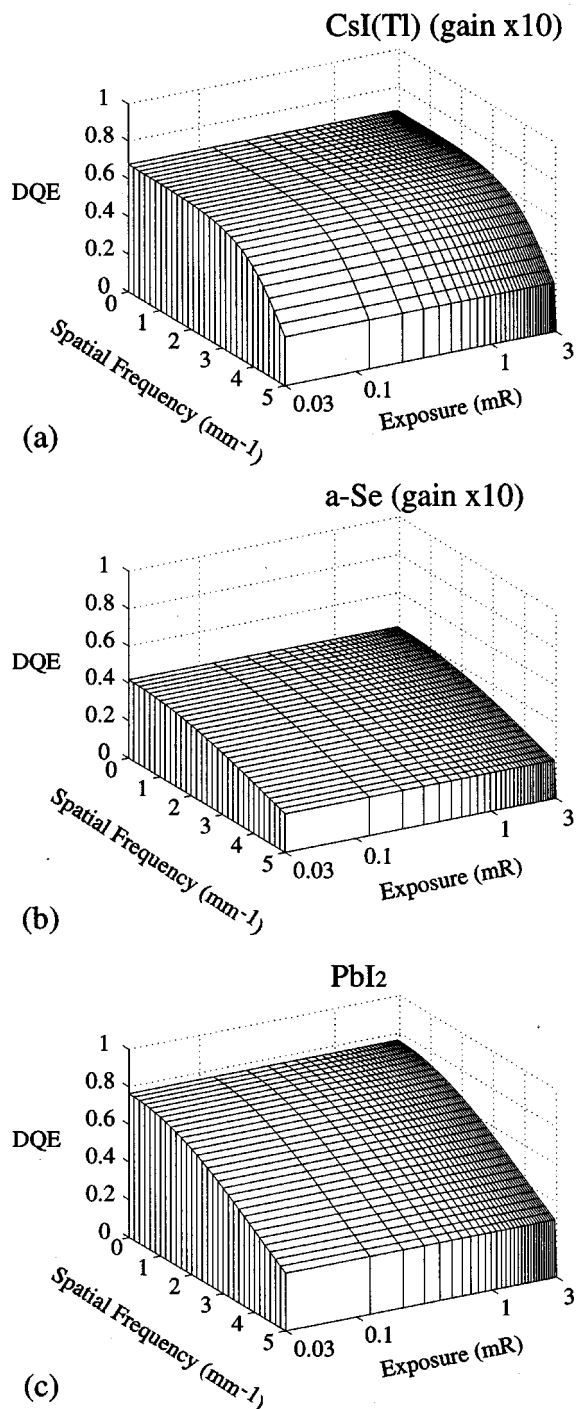

(a)

a-Se (gain x10)

(b)

PbI2

(c)

Fig. 13. Plot of DQE as a function of spatial frequency and exposure, based on Eqs. (6a) and (6b). The calculations are for advanced AMFPI designs with a 100 μm pixel pitch operated at full resolution at an energy of 110 kVp. The range of exposures corresponds to that associated with radiography while the spatial frequencies extend up to the Nyquist limit, 5 lp/mm. Calculations are shown for (a) CsI(Tl) and (b) *a*-Se designs, both with a pixel amplifier, and for (c) a PbI$_2$ design.

VI. SUMMARY AND DISCUSSION

Thin-film technology currently allows the creation of indirect detection and direct detection active matrix flat-panel imagers that offer many advantages for medical (and non-

medical) applications. However, theoretical analysis of the performance of systems whose design parameters are consistent with conventional (i.e., present day) AMFPIs indicates significant reductions in detective quantum efficiency under conditions of low exposure, such as is encountered in fluoroscopy. This analysis, which is based on the cascaded systems formalism, indicates that the origin of these reductions is the relatively large size of the total additive noise squared relative to the gain of the system. In order to address this problem, a variety of strategies have been presented in this paper that have the potential to significantly reduce additive noise and increase system gain. Strategies for additive noise reduction include careful pixel design to minimize TFT thermal noise, improved array and preamplifier design to decrease preamplifier noise, and the incorporation of compensation lines to diminish line noise. Strategies for system gain enhancement include use of continuous photodiode surfaces (for indirect detection designs), incorporation of an amplifier circuit in each pixel (for indirect or direct detection designs), or the use of a high sensitivity detection material such as PbI$_2$.

The effects upon the DQE performance for a variety of hypothetical (advanced) systems incorporating various combinations of these strategies have been quantitatively examined through cascaded systems model calculations. Such calculations can provide valuable insight into factors affecting DQE through clear illustration of trends in the functional dependence on variables such as exposure, spatial frequency, system design parameters, and operational conditions. Conversely, given the sensitivity of these calculations to choices made for the various parameters (e.g., the thickness of the x-ray converter), it would be unwarranted in the present context to place too much emphasis on the exact magnitude of the predicted DQE values for a given design.

The calculations predict that significant improvements in DQE performance can be achieved though introduction of design innovations that decrease total additive noise (particularly for devices with system gain representative of conventional technology) or increase system gain (e.g., by a factor of 10). In addition, the calculations indicate that strategies which provide both lower additive noise and high system gain result in DQE performance which is almost independent of exposure (even at the very low exposure levels associated with fluoroscopy) and which declines relatively slowly with increasing spatial frequency (under most conditions). Further, these improved levels of performance are predicted to degrade only relatively slowly with incremental increases in the total additive noise beyond the levels assumed in the present calculations. The calculations also indicate that for AMFPI systems whose gain is significantly enhanced (e.g., by a factor of 10), achieving a very high collection fill factor is far more critical for direct detection systems than for indirect detection systems.

Calculations for a variety of 100 μm pixel pitch designs offering low additive noise and high system gain suggest that such systems are capable of offering high and very similar levels of DQE performance over the wide range of exposure conditions representative of radiography and fluoroscopy. In

addition, the calculations also suggest that even at low exposures, advanced design AMFPIs could be operated at variable levels of resolution, via simultaneous readout of multiple gate lines, without substantial loss of DQE. Such constancy of performance would be beneficial when AMFPIs are operated fluoroscopically so as to provide digital zoom or high frame rates. Of course, even if DQE levels are nearly equivalent for fluoroscopic and radiographic conditions, the larger number of x-ray quanta available at the higher exposures associated with radiography will insure better image quality.

While the present calculations correspond to arrays having 20 cm long data lines, the weak dependence of preamplifier noise on line length (under the various assumptions of the current analysis) means that the DQE results presented in this paper would also largely apply for 40 cm arrays—a dimension of interest for fluoroscopic systems.[7,20] Present day systems achieve $40 \times 40 \, cm^2$ areas by tiling four $20 \times 20 \, cm^2$ arrays in a two by two pattern. While the use of smaller arrays is driven partially by considerations of cost of array manufacture, a smaller array also provides lower data line capacitance thereby reducing preamplifier noise. However, the use of multiple arrays for an imaging system has the disadvantage of increasing the number of channels of gate driver and preamplifier electronics since each array must be addressed separately. (The same general disadvantage also applies to an alternative strategy of physically cutting the data lines on a single large 40 cm array in two, making each side 20 cm long, in order to reduce the input capacitance to preamplifiers positioned on each end.) If, as is assumed in the present calculations, the data line capacitance can be significantly reduced, then a monolithic $40 \times 40 \, cm^2$ array having a single set of peripheral electronics would suffice and the challenges associated with mounting and aligning multiple arrays would be avoided.

The prospects and time scales for successful development of the various additive noise reduction and gain enhancement strategies presented in this paper vary widely. The noise reduction strategies (involving diminution of pixel storage capacitance and data line capacitance, improved preamplifier design, and incorporation of compensation lines for indirect detection arrays) are all under development and are expected to result in steadily improved noise performance over the next few years. Concerning the gain enhancement strategies, the success of a recent small area prototype[25] suggests that continued development and implementation of continuous photodiode surfaces in progressively larger indirect detection arrays is highly likely in the near future. The incorporation of amplifiers into the pixels will probably require considerably more time given the technological challenges involved. For example, while poly-Si TFTs are the preferred candidate for the amplifier circuit due to their higher mobility, their correspondingly higher leakage current makes them poor substitutes for the *a*-Si:H TFTs presently used as switches in the pixels. Thus, solutions such as poly-Si TFT pixel switches with lower leakage or hybrid thin-film processes capable of creating both poly-Si and *a*-Si:H TFTs in close proximity on the same substrate (possibly involving laser recrystallization

of *a*-Si) need to be developed. Efforts in this direction, as well as to increase the density of TFTs per unit area, are ongoing. Finally, the successful incorporation of PbI_2 as an x-ray converter for AMFPIs will necessitate continued development of this material. In particular, strategies to reduce the levels of the dark current of PbI_2 are needed and are under investigation as is the possibility of alternative converter materials.

While significant technical challenges remain to be addressed before many of the strategies presented in this paper can be implemented, the incentive for doing so is strong given the impressive improvements in DQE performance that appear possible. We anticipate that the coming decade will witness considerable progress toward the development of active matrix flat-panel imagers whose performance approach the theoretical limits.

ACKNOWLEDGMENTS

[a] Author to whom correspondence should be addressed. Phone: 734-936-4309; Fax: 734-936-7859; electronic mail: antonuk@umich.edu

[b] Presently at Department of Radiation Oncology, William Beaumont Hospital, Royal Oak, Michigan 48073.

[c] The scientific content of this paper was first presented at the SPIE Medical Imaging Conferences held in February 1998 and 1999 and at the annual meeting of the Radiological Society of North America in December 1998.

[1] R. A. Street, S. Nelson, L. E. Antonuk, and V. Perez Mendez, ''Amorphous silicon sensor arrays for radiation imaging,'' Mater. Res. Soc. Symp. Proc. **192**, 441–452 (1990).

[2] L. E. Antonuk, Y. El-Mohri, A. Hall, K.-W. Jee, M. Maolinbay, S. C. Nassif, X. Rong, J. H. Siewerdsen, Q. Zhao, and R. L. Weisfield, ''A large-area, 97 μm pitch, indirect-detection, active matrix flat-panel imager,'' Proc. SPIE **3336**, 2–13 (1998).

[3] R. A. Street, *Technology and Applications of Amorphous Silicon*, edited by R. A. Street, (Springer-Verlag, Berlin, 1999), Chap. 4, pp. 147–221.

[4] W. Zhao and J. A. Rowlands, ''X-ray imaging using amorphous selenium: Feasibility of a flat-panel self-scanned detector for digital radiology,'' Med. Phys. **22**, 1595–1604 (1995).

[5] D. L. Lee, L. K. Cheung, and L. S. Jeromin, ''A new digital detector for projection radiography,'' Proc. SPIE **2432**, 237–249 (1995).

[6] L. E. Antonuk, Y. El-Mohri, J. H. Siewerdsen, J. Yorkston, W. Huang, V. E. Scarpine, and R. A. Street, ''Empirical investigation of the signal performance of a high-resolution, indirect detection, active matrix flat-panel imager (AMFPI) for fluoroscopic and radiographic operation,'' Med. Phys. **24**, 51–70 (1997).

[7] J. Chabbal, C. Chaussat, T. Ducourant, L. Fritsch, J. Michailos, V. Spinnler, G. Vieux, M. Arques, G. Hahm, M. Hoheisel, H. Horbaschek, R. Schulz, and M. Spahn, ''Amorphous silicon x-ray image sensor,'' Proc. SPIE **2708**, 499–510 (1996).

[8] R. A. Street, R. B. Apte, S. E. Ready, R. L. Weisfield, and P. Nylen, ''Amorphous silicon sensor arrays for x-ray and document imaging,'' Mater. Res. Soc. Symp. Proc. **487**, 399–410 (1997).

[9] J. H. Siewerdsen, L. E. Antonuk, Y. El-Mohri, J. Yorkston, W. Huang, and I. A. Cunningham, ''Signal, noise power spectrum, and detective quantum efficiency of indirect-detection flat-panel imagers for diagnostic radiology,'' Med. Phys. **25**, 614–628 (1998).

[10] W. Zhao, I. Blevis, S. Germann, J. A. Rowlands, D. Waechter, and Z. Huang, ''Digital radiology using active matrix readout of amorphous selenium: Construction and evaluation of a prototype real-time detector,'' Med. Phys. **24**, 1834–1843 (1997).

[11] I. A. Cunningham, M. S. Westmore, and A. Fenster, ''A spatial-frequency dependent quantum accounting diagram and detective quantum

efficiency model of signal and noise propagation in cascaded imaging systems,'' Med. Phys. **21**, 417–427 (1994).

[12] J. H. Siewerdsen, L. E. Antonuk, Y. El-Mohri, J. Yorkston, W. Huang, J. M. Boudry, and I. A. Cunningham, ''Empirical and theoretical investigation of the noise performance of indirect detection, active matrix flat-panel imagers (AMFPIs) for diagnostic radiology,'' Med. Phys. **24**, 71–89 (1997).

[13] W. Zhao and J. A. Rowlands, ''Digital radiology using active matrix readout of amorphous selenium: Theoretical analysis of detective quantum efficiency,'' Med. Phys. **24**, 1819–1833 (1997).

[14] T. J. C. Bruijns, P. L. Alving, E. L. Baker, R. Bury, A. R. Cowen, N. Jung, H. A. Luijendijk, H. J. Meulenbrugge, and H. J. Stouten, ''Technical and clinical results of an experimental flat dynamic (digital) x-ray image detector (FDXD) system with real-time corrections,'' Proc. SPIE **3336**, 33–44 (1998).

[15] A. Tsukamoto, S. Yamada, T. Tomisaki, M. Tanaka, T. Sakaguichi, H. Asahina, and M. Nishiki, ''Development of a selenium-based flat-panel detector for real-time radiography and fluoroscopy,'' Proc. SPIE **3336**, 388–395 (1998).

[16] P. R. Granfors, ''Performance characteristics of an amorphous silicon flat panel x-ray imaging detector,'' Proc. SPIE **3659**, 480–490 (1999).

[17] A. Tsukamoto, S. Yamada, T. Tomisaki, M. Tanaka, T. Sakaguchi, H. Asahina, K. Suzuki, and M. Ikeda, ''Development and evaluation of a large-area selenium-based flat-panel detector for real-time radiography and fluoroscopy,'' Proc. SPIE **3659**, 14–23 (1999).

[18] L. E. Antonuk, Y. El-Mohri, W. Huang, K.-W. Jee, J. H. Siewerdsen, M. Maolinbay, V. E. Scarpine, H. Sandler, and J. Yorkston, ''Initial performance evaluation of an indirect-detection, active matrix flat-panel imager (AMFPI) prototype for megavoltage imaging,'' Int. J. Radiat. Oncol., Biol., Phys. **42**, 437–454 (1998).

[19] J. H. Siewerdsen and L. E. Antonuk, ''DQE and system optimization for indirect-detection flat-panel imagers in diagnostic radiology,'' Proc. SPIE **3336**, 546–555 (1998).

[20] U. Schiebel, N. Conrads, N. Jung, M. Weibrecht, H. Wieczorek, T. Zaengel, M. J. Powell, I. D. French, and C. Glasse, ''Fluoroscopic x-ray imaging with amorphous silicon thin-film arrays,'' Proc. SPIE **2163**, 129–140 (1994).

[21] M. J. Powell, C. Glasse, J. E. Curran, J. R. Hughes, I. D. French, and B. G. Martin, ''A fully self-aligned amorphous silicon TFT technology for large area image sensors and active-matrix displays,'' Mater. Res. Soc. Symp. Proc. **507**, 91–96 (1998).

[22] R. J. Yarema, T. Zimmerman, J. Srage, L. E. Antonuk, J. Berry, W. Huang, and M. Maolinbay, ''A programmable, low noise, multichannel preamplifier for pixelated amorphous silicon arrays,'' Nucl. Instrum. Methods **A439**, 413–417 (2000).

[23] I. Fujieda, R. A. Street, R. L. Weisfield, S. Nelson, P. Nylen, V. Perez-Mendez, and G. Cho, ''High sensitivity readout of 2D image sensors,'' Jpn. J. Appl. Phys. **32**, 198–204 (1993).

[24] L. E. Antonuk, J. Boudry, J. Yorkston, E. J. Morton, W. Huang, and R. A. Street, ''Development of thin-film, flat-panel arrays for diagnostic and radiotherapy imaging,'' Proc. SPIE **1651**, 94–105 (1992).

[25] J. T. Rahn, F. Lemmi, R. L. Weisfield, R. Lujan, P. Mei, J. Lu, J. Ho, S. E. Ready, R. B. Apte, P. Nylen, J. Boyce, and R. A. Street, ''High resolution, high fill factor *a*-Si:H sensor arrays for medical imaging,'' Proc,. SPIE **3659**, 510–517 (1999).

[26] L. E. Antonuk, Y. El-Mohri, K.-W. Jee, M. Maolinbay, S. C. Nassif, X. Rong, J. H. Siewerdsen, Q. Zhao, and R. A. Street, ''Beyond the limits of present active matrix flat-panel imagers (AMFPIs) for diagnostic radiology,'' Proc. SPIE **3659**, 518–527 (1999).

[27] G. Gho, J. S. Drewery, W. S. Hong, T. Jing, S. N. Kaplan, H. Lee, A. Mireshghi, V. Perez-Mendez, and D. Wildermuth, ''Signal readout in *a*-Si:H pixel detectors,'' IEEE Trans. Nucl. Sci. **40**, 323–327 (1993).

[28] N. Matsuura, W. Zhao, Z. Huang, and J. A. Rowlands, ''Digital radiology using active matrix readout: Amplified pixel detector array for fluoroscopy,'' Med. Phys. **26**, 672–681 (1999).

[29] F. Glasser, J. L. Martin, B. Thevenin, P. Schermesser, P. Pantigny, J. Y. Laurent, P. Rambaud, B. Pitault, and S. Paltrier, ''Recent developments on a CdTe based x-ray detector for digital radiography,'' Proc. SPIE **3032**, 513–519 (1997).

[30] K. S. Shah, P. Bennett, M. Klugerman, L. P. Moy, G. Entine, D. Ouimette, and R. Aikens, ''Lead iodide films for x-ray imaging,'' Proc. SPIE **3032**, 395–404 (1997).

[31] K. S. Shah, P. Bennett, L. Cirignano, Y. Dmitriyev, M. Klugerman, K. Mandal, L. P. Moy, and R. A. Street, ''Characterization of x-ray imaging properties of PbI_2 films,'' Mater. Res. Soc. Symp. Proc. **487**, 351–360 (1997).

[32] R. Street, K. Shah, S. Ready, R. Apte, P. Bennett, M. Klugerman, and Y. Dmitriyev, ''Large area x-ray image sensing using a PbI_2 photoconductor,'' Proc. SPIE **3336**, 24–32 (1998).

[33] J. Rowlands and S. Kasap S, ''Amorphous semiconductors usher in digital x-ray imaging,'' Phys. Today Nov. 24–30 (1997).

[34] I. A. Cunningham, ''Degradation of the detective quantum efficiency due to a non-unity detector fill factor,'' Proc. SPIE **3032**, 22–31 (1997).

[35] R. Birch, M. Marshall, and G. M. Ardran, ''Catalog of spectral data for diagnostic x rays,'' Hospital Physicists' Association, Scientific Report Series 30 (1979).

[36] E. Storm and H. I. Israel, ''Photon cross sections from 1 keV to 100 MeV for elements $Z=1$ to $Z=100$,'' Nucl. Data Tables **7**, 565–681 (1970).

[37] H. P. Chan and K. Doi, ''Energy and angular dependence of x-ray absorption and its effect on radiographic response in screen–film systems,'' Phys. Med. Biol. **28**, 565–579 (1983).

[38] R. Fahrig, J. A. Rowlands, and M. J. Yaffe, ''X-ray imaging with amorphous selenium: Detective quantum efficiency of photoconductive receptors for digital mammography,'' Med. Phys. **22**, 153–160 (1995).

[39] N. Jung, P. L. Alving, F. Busse, N. Conrads, H. M. Meulenbrugge, W. Rutten, U. Schiebel, M. Meibrecht, and H. Wieczorek, ''Dynamic x-ray imaging system based on an amorphous silicon thin-film array,'' Proc. SPIE **3336**, 396–407 (1998).

[40] L. E. Antonuk, J. Yorkston, W. Huang, J. Siewerdsen, and R. A. Street, ''Considerations for high frame rate operation of two-dimensional *a*-Si:H imaging arrays,'' Mater. Res. Soc. Symp. Proc. **297**, 945–950 (1993).

[41] R. A. Street, J. T. Rahn, S. E. Ready, K. Shah, P. R. Bennett, Y. Dmitriyev, P. Mei, J.-P. Lu, R. B. Apte, J. Ho, K. van Schuylenbergh, F. Lemmi, J. B. Boyce, and P. Nylen, ''X-ray imaging using lead iodide as a semiconductor detector,'' Proc. SPIE **3659**, 36–47 (1999).

[42] M. J. Berger and J. H. Hubbell, ''XCOM: Photon cross sections on a personal computer,'' NIST internal Report NBSIR 87-3597, 1987.

[43] W. Zhao and J. A. Rowlands, ''A large area solid-state detector for radiology using amorphous selenium,'' Proc. SPIE **1651**, 134–143 (1992).

[44] D. J. Robbins, ''On predicting the maximum efficiency of phosphor systems excited by ionizing radiation,'' J. Electrochem. Soc. **127**, 2694–2702 (1980).

[45] H. E. Johns and J. R. Cunningham, *The Physics of Radiology*, 4th ed. (Charles C. Thomas, Illinois, 1983), pp. 558–563.